The Diurnal Cycle of Entrainment and Detrainment in LES of the Southern Ocean Driven by Observed Surface Fluxes and Waves

WILLIAM G. LARGE,[a] EDWARD G. PATTON,[a] AND PETER P. SULLIVAN[a]

[a] *National Center for Atmospheric Research, Boulder, Colorado*

(Manuscript received 21 December 2020, in final form 21 July 2021)

ABSTRACT: Empirical rules for both entrainment and detrainment are developed from LES of the Southern Ocean boundary layer when the turbulence, stratification, and shear cannot be assumed to be in equilibrium with diurnal variability in surface flux and wave (Stokes drift) forcing. A major consequence is the failure of downgradient eddy viscosity, which becomes more serious with Stokes drift and is overcome by relating the angle between the stress and shear vectors to the orientations of Lagrangian shear to the surface and of local Eulerian shear over 5 m. Thus, the momentum flux can be parameterized as a stress magnitude and this empirical direction. In addition, the response of a deep boundary layer to sufficiently strong diurnal heating includes boundary layer collapse and the subsequent growth of a morning boundary layer, whose depth is empirically related to the time history of the forcing, as are both morning detrainment and afternoon entrainment into weak diurnal stratification. Below the boundary layer, detrainment rules give the maximum buoyancy flux and its depth, as well a specific stress direction. Another rule relates both afternoon and nighttime entrainment depth and buoyancy flux to surface layer turbulent kinetic energy production integrals. These empirical relationships are combined with rules for boundary layer transport to formulate two parameterizations; one based on eddy diffusivity and viscosity profiles and another on flux profiles of buoyancy and of stress magnitude. Evaluations against LES fluxes show the flux profiles to be more representative of the diurnal cycle, especially with Stokes drift.

KEYWORDS: Boundary layer; Langmuir circulation; Oceanic mixed layer; Large eddy simulations; Parameterization

1. Introduction

Studies of the upper ocean advance the understanding necessary to develop rules relating the turbulence to the forcing and the ocean state. These mixing rules allow turbulent fluxes to be estimated from information provided by observations, numerical models, or a combination of both through data assimilation. Unfortunately, the technology to measure fluxes directly in the open ocean does not yet exist, so observational knowledge is limited to indirect inferences, such as those from ocean microstructure (e.g., Moum et al. 2013).

In ocean general circulation models vertical mixing schemes employ a set of established rules to parameterize the vertical fluxes, whose divergences appear as terms in the prognostic equations for the resolved ocean state. Such schemes come in two distinct flavors, that Burchard et al. (2008) term statistical turbulence models (STM) and empirical turbulence models (ETM). STMs solve the Reynolds-averaged Navier–Stokes equations with a variety of second-order closures (e.g., Mellor and Yamada 1982; Kantha and Clayson 1994; Harcourt 2015) and some higher order (e.g., Cheng et al. 2002; Canuto et al. 2009). Empirical relationships simplify ETMs, such as the mixed-layer models of Kraus and Turner (1967) lineage, and of Price et al. (1986) and the *K*-profile parameterization (KPP) of the ocean boundary layer (Large et al. 1994). In the absence of direct measurements, evaluation of all schemes, as well as guidance on further developments, have relied heavily on comparisons of modeled and observed ocean states. However, discrepancies are caused both by inadequate rules and by forcing error, with no means to discriminate and the possibility of compensating errors a further complication.

An extensive comparison by Li et al. (2019) of 11 vertical mixing schemes, including both STM and ETM, demonstrates the current lack of community consensus. The primary metric is the mixed layer depth (MLD) of de Boyer Montégut (2004), and a robust conclusion is that the inclusion of Langmuir turbulence produces deeper MLD. Although this measure would be insufficient for either showing comprehensive agreement or for judging relative merit, it does expose "limited understanding and numerical deficiencies." In particular, no two schemes agree globally over the annual cycle, so overall they do not perform as well as might be expected based on the theory, observations, and numerical experiments applied to their development. One of the focused demonstrations of disparate behavior is the annual cycle at Ocean Weather Station Papa, but unbalanced surface fluxes preclude the quantitative evaluations against observations of both the forcing and ocean state found in Martin (1985) and Large (1996), for example.

Large-eddy simulation (LES) is fundamentally different and offers unique opportunities, because it can be used to study turbulence (Burchard et al. 2008). LES models solve the Navier–Stokes equations by resolving the vertical fluxes down to scales of order a meter, such that subgrid-scale (SGS) contributions are small and relatively well parameterized. LES is key to many recent advances in the understanding and hence modeling of upper-ocean mixing physics (e.g., McWilliams et al. 1997; Wang et al. 1998; Grant and Belcher 2009; Harcourt and D'Asaro 2008; van Roekel et al. 2012; Li and Fox-Kemper 2017).

Denotes content that is immediately available upon publication as open access.

Corresponding author: W. G. Large, wily@ucar.edu

DOI: 10.1175/JPO-D-20-0308.1

The present study of the diurnal cycle follows directly from two particular examples: Large et al. (2019a, hereafter L19a) extends Monin–Obukhov similarity theory (Monin and Obukhov 1954) to include surface wave forcing (Stokes drift), and Large et al. (2019b, hereafter L19b) relates this forcing to both the local and the nonlocal transports of buoyancy and momentum throughout the boundary layer. Hereafter, these works will collectively be referred to as L19. These results and additional analyses of the same LES data (Large et al. 2021) are herein combined to develop rules for boundary layer entrainment and detrainment and for misalignment of the shear and turbulent stress vectors when changes in the forcing may be too rapid for equilibrium assumptions.

The LES model, the surface flux and wave forcing, and the various simulations are detailed L19, so only the most relevant aspects are recapped in section 2. Germane results from L19 are summarized in section 3, where there is also a novel analysis of similarity theory in the stably forced surface layer. In section 4, an empirical rule that includes Stokes forcing is developed for entrainment into both convective nighttime and stable afternoon boundary layers. In addition, the orientation of the stress vector is related to the Eulerian and Lagrangian shear over different vertical scales. Section 5 focuses on detrainment, which is broadly defined as daytime turbulence that depends strongly on past history, such as found below a stable morning boundary layer. In section 6, the diurnal cycles of buoyancy and momentum fluxes in the upper ocean are parameterized in two distinct ways, then both are evaluated against LES fluxes to take advantage of the LES mean ocean state and turbulence statistics being consistent with the specified "error-free" forcing.

2. LES of the Southern Ocean boundary layer

Large-eddy simulations of the ocean boundary layer are driven by the observed forcing shown in Fig. 1 at the Southern Ocean Flux Site (SOFS) near 47°S, 140°E (Schultz et al. 2012). As detailed in L19a, there are two cases from April 2010: AprS with wave forcing from realistic Stokes drift profiles and AprN without. Two additional cases from June 2010 are similarly denoted as JunS and JunN. Also utilized here is an idealized case, D24S, where the surface waves are always perfectly aligned with a westerly wind. All cases use the SOFS inertial period of 16.4 h. This study of the diurnal cycle focuses on AprS, because it is the only Stokes case with a period of surface buoyancy gain (Fig. 1c), beginning with the transition at $t_{\rm US} = 32.75$ h from unstable buoyancy forcing (effective cooling) to stable (heating), until the reverse at $t_{\rm SU} = 40.75$ h. The other cases extend the range of forcing conditions, including the prior April diurnal cycle, as well as another two in June (noon at hours 6 and 30) when there is net cooling throughout.

The LES model is well documented (Moeng 1984; Sullivan et al. 1994; McWilliams et al. 1997) and widely used in ocean boundary layer studies (e.g., Sullivan et al. 2012; van Roekel et al. 2012; Kukulka et al. 2013). The modifications to account for surface wave effects are extensive and summarized in L19a, as are the initial conditions and grid choices. Initially, the inversion depth of maximum stratification d_i is about 180 m in April, 222 m in June, and 96 m for D24S. The model solves the wave-averaged, incompressible, and Boussinesq Craik–Leibovich equation set (Craik and Leibovich 1976; McWilliams et al. 1997). Its thermodynamic variable is buoyancy $g(1 - \rho/\rho_o)$, relative to a reference density ρ_o, where g is gravitational acceleration and ρ is ocean density. It produces evolving profiles of horizontal and time mean buoyancy Θ and horizontal Eulerian flow $\mathbf{U}$, with orthogonal components, U and V. The corresponding turbulent vertical fluxes, $\langle w\theta\rangle$, $\langle wu\rangle$, and $\langle wv\rangle$, are given by the correlations of vertical velocity w with fluctuations, θ, u, and v, plus small SGS contributions. Similarly, the variance of velocity fluctuations plus SGS give the turbulent kinetic energy, TKE, whose dissipation $\varepsilon_{\rm TKE}$ is parameterized. Hourly statistics converge and are computed half-hourly in order to track turbulent responses to the variable forcing that are faster than the responses of stratification and shear, and hence of eddy diffusivity and viscosity. Thus, only every second calculation is independent.

a. Meteorological and Stokes (wave) forcing

The surface wind stress divided by ρ defines the kinematic wind stress $\boldsymbol{\tau}_0$ whose magnitude is the friction velocity u^{*2}, with an April range in Fig. 1a corresponding to wind speeds from about 3 to 20 m s^{-1}. The wind direction of Fig. 1b is in degrees clockwise from north and there is always an eastward (westerly) component. The surface buoyancy flux B_0 includes both heat and freshwater forcing, and defines the equivalent heating of Fig. 1c:

$$Q_0 = \frac{\rho C_p}{g\alpha} B_0, \tag{1}$$

where thermal expansion is constant at $\alpha = 1.7 \times 10^{-4}\,\mathrm{K}^{-1}$, and C_p is ocean heat capacity, with $\rho C_p = 4.2\,\mathrm{MJ\,m^{-3}\,K^{-1}}$. The maximum heating of 200 W m^{-2} is much less than reached at noon in summer or at low latitudes, when the simplification of absorbing all the solar radiation in the first model level would not be as defensible.

Surface waves are imposed as profiles of Stokes drift $\mathbf{U}_S(z)$, computed from simulated, high-resolution directional wave height spectra, as detailed in L19a. The Lagrangian current is $\mathbf{U}_L(z) = \mathbf{U}_S(z) + \mathbf{U}(z)$. The turbulent Langmuir number (La) of McWilliams et al. (1997) is defined such that ${\rm La}^{-2} = |\mathbf{U}_S(0)|/u^*$, which fluctuates by ± 5 about its wind-wave equilibrium value of 11 (L19).

The surface layer extends to a fraction, $\varepsilon = 0.1$, of a boundary layer of depth h. In L19a, surface wave effects are incorporated into Monin–Obukhov similarity theory by regarding the sources of TKE over this layer as a forcing. Specifically, the contributions of Eulerian shear, Stokes shear, and buoyancy are given by the integrals

$$\int_{-\varepsilon h}^{0} (\langle -w\mathbf{u}\rangle \cdot \partial_z \mathbf{U})\, dz = P_U u^{*3}, \tag{2}$$

$$\int_{-\varepsilon h}^{0} (\langle -w\mathbf{u}\rangle \cdot \partial_z \mathbf{U}_S)\, dz = P_S u^{*2} |\mathbf{U}_S(0)| = P_S {\rm La}^{-2} u^{*3}, \tag{3}$$

$$\int_{-\varepsilon h}^{0} (\langle w\theta\rangle)\, dz = P_B B_0 h = P_B w^{*3}, \tag{4}$$

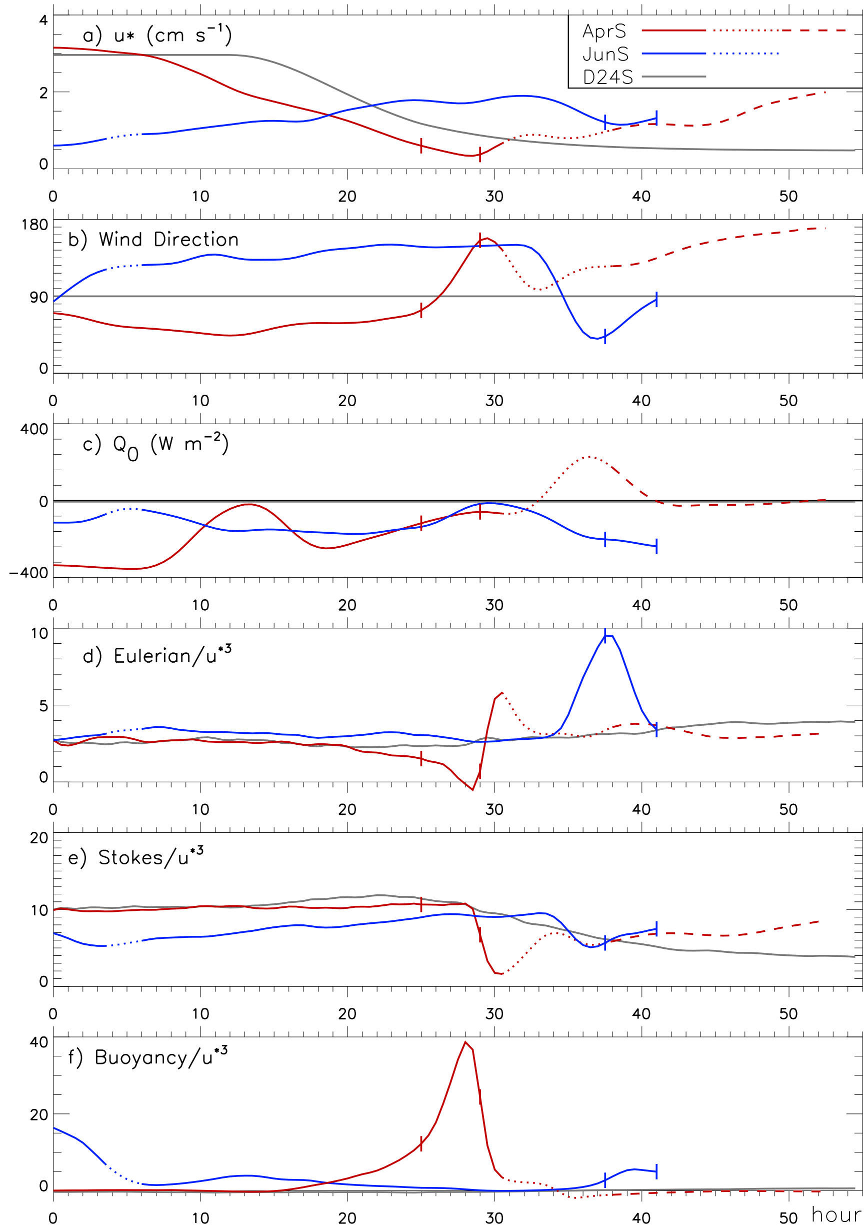

FIG. 1. SOFS surface forcing for April (red) and June (blue), and the idealized forcing of D24S (gray): (a) friction velocity u^*; (b) the direction to which the wind blows in compass degrees from north; and (c) the surface buoyancy flux B_0 as an equivalent surface heating Q_0 from (1). The normalized integrated TKE production, or suppression above the inversion depth d_i normalized by u^{*3}, due to (d) Eulerian shear, (e) Stokes shear, and (f) buoyancy. Each time series reflects regimes E_C (solid), DBL plus SBL (dotted), and E_W (dashed), with vertical bars demarking the WRW and MRW periods of counterinertial wind rotation.

respectively, over depths where the TKE production terms in square brackets are positive sources, but not negative sinks. The above scaling with u^*, La, and the convective velocity scale w^* defines the three coefficients P_U, P_S, and P_B, that are parameterized in L19a, with updates coming in section 6.

Figure 2 shows the AprS distributions below 1 m of TKE, its dissipation, and its three production terms of both signs. The column integrals of these three terms above the inversion depth (Fig. 2d) are displayed as time series in Fig. 1. The buoyancy integral is often small (Fig. 1f), because of significant TKE suppression ($\langle w\theta \rangle < 0$), and can become negative with heating ($Q_0 > 0$). Usually the column Eulerian production is about $3u^{*3}$ (Fig. 1d), and one-half to one-third that of the Stokes (Fig. 1e). However, these balances are upset by variable forcing. In particular, the period of weakest winds ($u^* < 0.6\,\mathrm{cm\,s^{-1}}$) of AprS is between hours 25 and 30 and coincides with a shift in

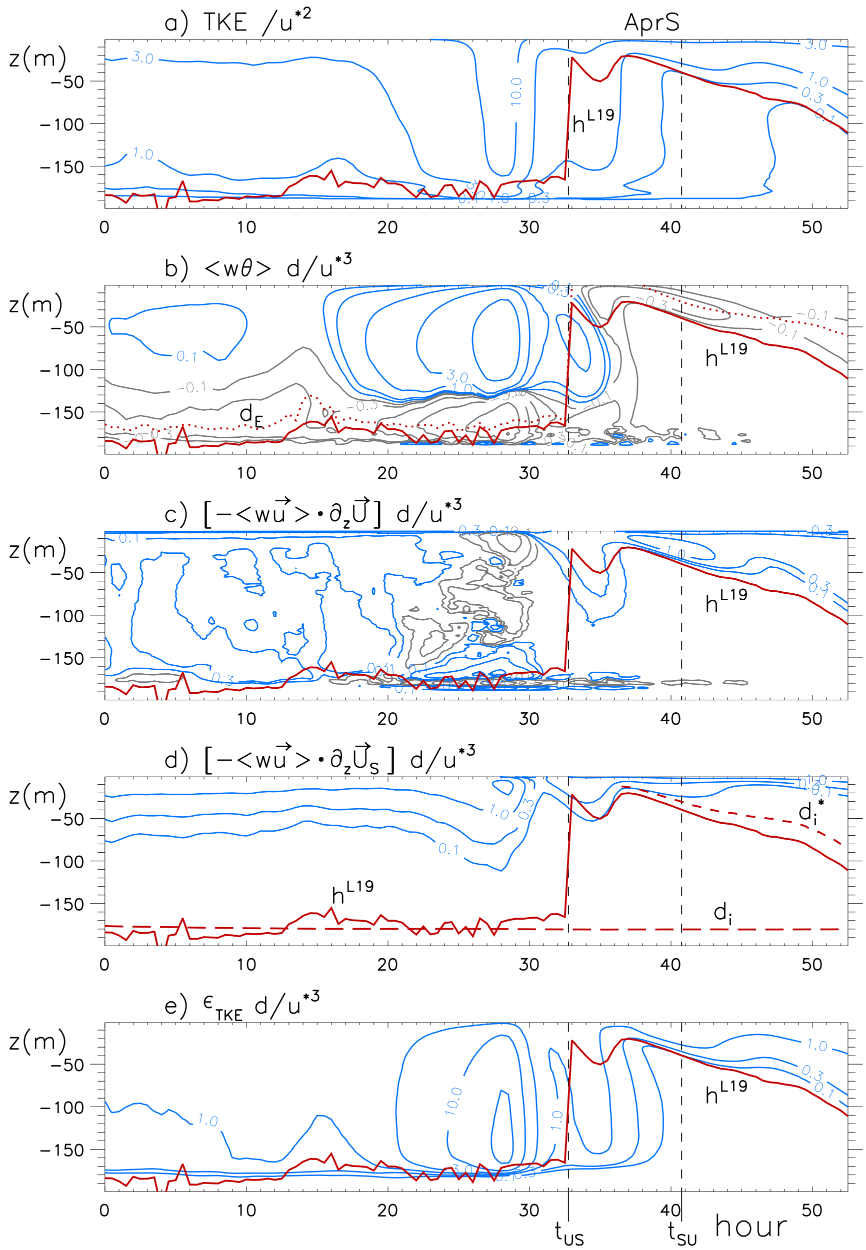

FIG. 2. The AprS nondimensional distributions below 1 m of (a) TKE and its (b) buoyancy production, (c) Eulerian shear production, (d) Stokes shear production, and (e) dissipation. The contours are irregular at ±0.10, ±0.30, ±1.0, ±3.0, ±10.0, and 30, with negative contours gray. The time series (red) show the boundary layer depth h^{L19} (solid), the entrainment depth d_E (dotted line), the inversion depth d_i (long-dashed line) of maximum stratification, and d_i^* (short-dashed line) where stratification is a local maximum in regime E_W. The vertical dashed lines demark the stable forcing between t_{US} and t_{SU}.

wind direction of about 80° from nearly eastward to almost southward. This counterinertial rotation has profound effects on the dot product of Fig. 2c, such that Eulerian shear becomes a net sink of TKE in Fig. 1d, and buoyancy the dominant source. This peculiar combination of weak rotating wind will be referred to as the WRW period. It ends abruptly when the wind strengthens, its rotation reverses and approaches the inertial rate of $-22° \mathrm{h}^{-1}$, and the Eulerian shear production rapidly increases. There is a similar response prior to hour 37 in June, followed by the MRW period of moderate winds and counterinertial rotation.

b. *Diagnostic depths, regimes, and layers*

Surface forced turbulence, including Stokes effects, dominates at depths, $d = -z$, in the boundary layer where $\sigma = d/h$

TABLE 1. Catalog of depths and of angles between horizontal vectors, including empirical relationships, brief descriptions, basic dependencies, and references.

		Dependencies	References
Depths			
d_i	Inversion depth of maximum stratification	Θ	Fig. 2d
d_i^*	Depth of local maximum stratification	Θ	Figs. 2d and 3
d_E	Entrainment depth of minimum buoyancy flux, $B_E < 0$	$\langle w\theta\rangle$	Figs. 2b and 3
h^{L19}	Approximate boundary layer depth from L19	$\langle w\theta\rangle$	Fig. 2
h^{KPP}	KPP boundary layer depth	Θ; $\mathbf{U}$; forcing	Danabasoglu et al. (2006)
d_{MAX}	Detrainment depth of maximum positive buoyancy flux	$\langle w\theta\rangle$	Fig. 9
d_{MKE}	Depth of minimum mean kinetic energy	$\mathbf{U}$	Fig. 9
L^*	Modified Monin–Obukhov depth	Forcing	Eq. (14); Fig. 9
MLD*	Mixed layer depth (small threshold)	Θ	Fig. 13c
Empirical			
h^{BL}	Entraining boundary layer depth	d_E; forcing; Θ	Fig. 7
$h^{\mathrm{AM}}(t)$	Depth of growing stable morning boundary layer	Forcing	Eq. (21); Fig. 9
h	Boundary layer depth of choice	h^{BL}; h^{AM}	Figs. 9 and 13a
d_E^{ER}	Parameterized entrainment depth	Forcing; Θ	Eq. (17); Fig. 7
h^{ER}	Parameterized boundary layer depth	Forcing; Θ	Fig. 7
h^{PAR}	Merged parameterized boundary layer depth	h^{ER}; h^{AM}; κL^*	Fig. 13b
$d_{\mathrm{MAX}}(t)$	Time integrated detrainment depth	Forcing	Eq. (22); Fig. 9
$-z_D$	Extent of detrainment zone	$d_E^{\mathrm{ER}}(t_{\mathrm{ED}})$	Eq. (23); Table 2
Angles			
Ω	Stress from shear	$\langle w\mathbf{u}\rangle$; $\mathbf{U}$	L19b
Ω_W	Wind from shear	$\boldsymbol{\tau}_0$; $\mathbf{U}$	L19b
Ω_τ	Stress from wind	$\Omega - \Omega_W$	Figs. 8 and 10
Empirical			
$\Omega_\tau^{\mathrm{BL}}$	Boundary layer parameterized stress from wind	$\boldsymbol{\tau}_0$; $\mathbf{U}$; $\mathbf{U}_S$	Eq. (20)
$\Omega_\tau^{\mathrm{DZ}}$	Detrainment-zone parameterized stress from wind	Ω_W; $\mathbf{U}$	Eq. (24)

is a natural vertical coordinate. Table 1 catalogs various boundary layer depths as well as other diagnostic and empirical depths and angles. In L19, the buoyancy flux (e.g., Fig. 2b) is used to diagnose the entrainment depth (d_E, dotted red trace) where the entrainment buoyancy flux B_E is a negative minimum, as well as a deeper boundary layer depth h^{L19} (solid red traces) where the flux approaches a local maximum, which is usually near zero. However, when the surface forcing does not dominate, this maximum can be shallow and significantly positive, such that the boundary layer and interpretation of h^{L19} become ambiguous. In particular, Fig. 2b shows a very abrupt collapse of h^{L19} at t_{US}, followed by two hours of deepening then 2 h of shoaling, but this behavior is reflected in neither TKE (Fig. 2a), nor its dissipation (Fig. 2e).

The examples of Fig. 3 show profiles of buoyancy flux (blue traces) and smoothed stratification (red traces). The stratification is scaled with depth, so it is constant where the buoyancy profile is logarithmic. The additional scaling by $u^*/|B_0|$ in the upper panels gives the traditional nondimensional gradient, divided by the von Kármán constant, $\kappa = 0.4$, but becomes $10^5/g$ in the lower, in order to capture transitions across $B_0 = 0$, and to display the local diurnal maximum at depths, $d_i^* < h^{\mathrm{L19}} \ll d_i$. With either scaling the column maximum at d_i is more than 1000 and far off scale. These examples demonstrate that the diurnal cycle can be partitioned into at least four regimes, namely, a stable boundary layer (SBL), a detraining boundary layer (DBL), wind/wave dominated entrainment (E_W), and the most common regime E_C (Fig. 1; solid) when convective entrainment is more important. The familiar partition into unstable and stable boundary layers does not capture the diurnal cycle, because detrainment (regime DBL) becomes evident prior to t_{US} as the dominance of surface forcing diminishes, and characteristics of stable afternoon entrainment (regime E_W) can persist well past t_{SU}.

Both entrainment regimes are characterized by buoyancy loss ($\partial_z\langle w\theta\rangle > 0$) between the surface and d_E and by gain below as denser water is mixed into the boundary layer. Regime E_C covers convective entrainment into strong stratification near the inversion. In the typical example of Fig. 3a, stratification is unstable above 80 m and the nearly logarithmic buoyancy profile is consistent with similarity theory even beyond the surface layer. Also, $\langle w\theta\rangle$ is countergradient between 75 and 100 m. Apart from the WRW period, Fig. 2 shows that TKE scales well with u^{*2} and depth relative to h^{L19}, Stokes shear production dominates near the surface, and scaled dissipation over the upper half of the boundary layer decreases steadily from about $\kappa^{-1} = 2.5$ at the surface to about 1.

The onset of solar radiation, with weak winds initiates a transition from regime E_C to DBL at time, $t_{\mathrm{ED}} = 30.5$ h of AprS. Regime DBL has unstable forcing ($B_0 < 0$) to t_{US} and lasts until a transition to regime SBL at about $t_{\mathrm{DS}} = 35.5$ h. The profiles of Fig. 3b are representative of the entire regime, including a period of JunS (Fig. 1; dotted blue). The robust characteristics of detrainment are negligible entrainment; negative curvature of the buoyancy flux profile in a detrainment zone from the surface to near the entrainment depth at

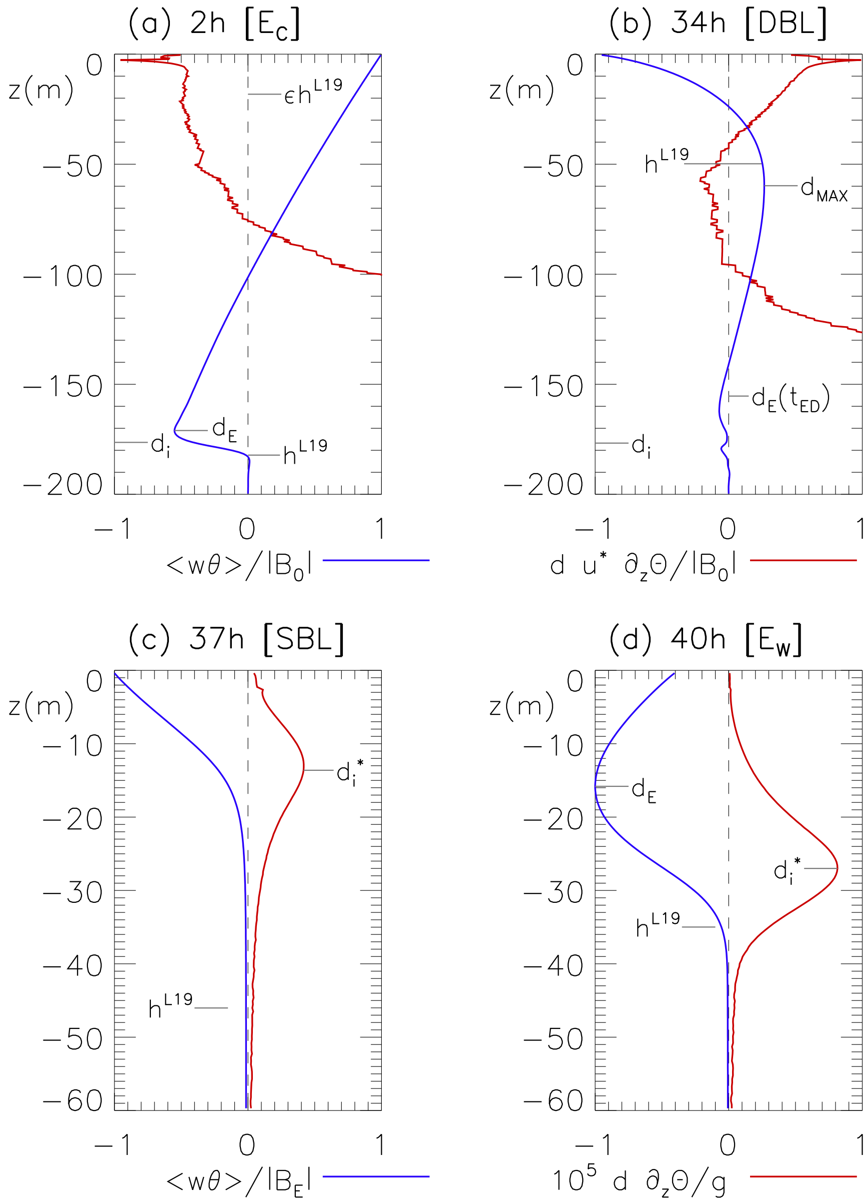

FIG. 3. Profiles of buoyancy flux (blue) normalized by the greater of $|B_0|$ or $|B_E|$, and of smoothed stratification (red) scaled (top) by $du^*/|B_0|$ or (bottom) by $10^5 d/g$ from AprS regimes: (a) E_C at hour 2, (b) DBL at hour 34, with the entrainment depth at $t_{ED} = 30.5$ h, (c) SBL at hour 37 ($B_E = -B_0$), and (d) E_W at hour 40. The depths are described in Table 1.

the transition [$d_E(t_{ED})$ about 155 m]; h^{L19} approaches the depth d_{MAX} where the flux is a positive maximum denoted as B_{MAX}; no logarithmic layer above h^{L19}; and extensive regions of countergradient buoyancy flux both above and below d_{MAX}. In Fig. 2b, d_{MAX} steadily deepens from the surface at t_{ED} to about 100 m at t_{DS}, while TKE/u^{*2} decreases, Stokes production is less than Eulerian and scaled dissipation is about 1. Combined, these features suggest the influence of prior convective turbulence throughout the detrainment zone.

The Fig. 3c example from regime SBL (from t_{DS} until the transition to regime E_W at $t_{SE} = 38.5$ h) appears to be a near equilibrium stable boundary layer, because there is no evidence of either entrainment ($d_E = 0$), or detrainment ($B_{MAX} \leq 0$). Its characteristic depth is relatively shallow, with d_i^* only about 15 m. Figure 3d is representative of subsequent entrainment into this shallow diurnal stratification during regime E_W when the wind–wave forcing and diurnal shear overcome the afternoon surface buoyancy gain and stop the diurnal sea surface temperature warming in early afternoon (e.g., Filipiak et al. 2012; Large and Caron 2015). This entrainment continues after t_{SU}, while buoyancy forcing remains negligible, and deepens d_i^* to about 80 m (Fig. 2d; short-dashed line). Regime

E_W (Fig. 3d) is also distinguished from regime E_C, by evidence of neither a logarithmic profile, nor countergradient buoyancy flux.

3. The upper-ocean boundary layer

Following L19, a useful construct for a surface forced boundary layer ($\sigma < 1$) is to express the turbulent vertical fluxes as a local downgradient flux proportional to the local vertical gradient plus a nonlocal term representing everything else. For buoyancy this partition gives

$$\langle w\theta\rangle = K_s(-\partial_z\Theta) + \Gamma_\theta = K_s(-\partial_z\Theta + \gamma_\theta), \quad (5)$$

where K_s is an eddy diffusivity and $-\gamma_\theta$ is the effective nonlocal buoyancy gradient (Deardorff 1972). Furthermore, L19b finds that there is usually a nonzero angle Ω of the kinematic turbulent stress $\boldsymbol{\tau}$ from the Eulerian shear vector and a different angle Ω_W of the wind from the shear (Table 1). In the coordinate system with the U current component aligned with this shear and V orthogonal, $\partial_z V$ is zero and the partition becomes

$$\langle wu\rangle = K_m(-\partial_z U) + \Gamma_u = K_m(-\partial_z U + \gamma_u) = -\tau\cos\Omega;$$

$$\langle wv\rangle = \Gamma_v = -\tau\sin\Omega, \quad (6)$$

where K_m is an eddy viscosity, $-\gamma_u$ is an effective nonlocal shear, and the momentum flux vector is $\langle w\mathbf{u}\rangle = -\boldsymbol{\tau}$. Using the subscript ($m$, s) to refer to momentum or scalars, a general form for boundary layer viscosity and diffusivity is

$$K_{m,s}(\sigma) = w_{m,s}hG_{m,s}(\sigma) = \frac{\kappa u^*}{\phi_{m,s}(\zeta)\chi_{m,s}(\xi)}\,h\,G_{m,s}(\sigma), \quad (7)$$

which defines the turbulent velocity scales, $w_{m,s}$, whose L19a parameterizations are updated in section 6a. The similarity functions $\phi_{m,s}$ and $\chi_{m,s}$ are formulated in section 3a.

The nondimensional shape functions $G_{m,s}$ are found to be quite similar in L19b, and the combined averages over 20 bins are shown in Fig. 4 (G_C^{L19}; black squares). For present purposes a composite shape function, G_C (black trace) is constructed. It is the piecewise linear interpolation between G_C^{L19} for σ between 0.05 and 0.525. Nearer the surface (bottom panel), $G_C = \sigma(1 - 3\sigma)$, such that $G_C/\sigma \to 1$ at the surface. Deeper, the behavior of G_s affects entrainment, so it is revisited in Fig. 4 (top panel). For $\sigma > 0.525$, the composite becomes $G_C = 0.287(1 - \sigma)^2$. This quadratic is a very good fit to the L19b bin averages of G_m (red crosses) from the Stokes cases and it falls well within a standard deviation of the G_s bin averages from all cases (blue diamonds). However, it lies systematically below G_C^{L19}, because of high values of $G_m > G_C > G_s$ from AprN and JunN, but these cases are not a present focus.

From L19b, the dependencies of Γ_θ in (5) and Γ_v in (6) are similar to buoyancy in the convective atmospheric boundary layer, with $\Gamma_\theta = 0$ in the stable:

$$\Gamma_\theta = R_s\,G_C(\sigma)\frac{(|B_0| - B_0)}{2}; \qquad \Gamma_v = R_m\,G_C(\sigma)\,u^{*2}\sin(-\Omega_W), \quad (8)$$

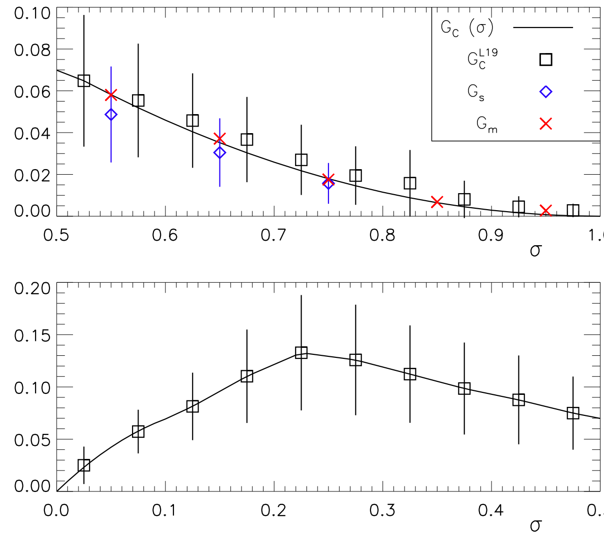

FIG. 4. Nondimensional shape functions of (top) $\sigma > 0.5$ and (bottom) $\sigma < 0.5$: the revised composite G_C (solid black traces); and the composite bin averages G_C^{L19} from L19b (black squares). The upper panel compares G_m from the Stokes forced cases of L19b (red crosses), including AprS, and G_s from all cases of L19b (blue diamonds). Vertical bars extend ± 1 standard deviation from G_C^{L19} and G_s.

where the shear is $(-\Omega_W)$ from the wind and the empirical coefficients are $R_m = 3.5$ and $R_s = 4.7$.

The surface layer

The surface layer above (εh) has distinctive physics described by semiempirical Monin–Obukhov similarity theory. Following L19a, nondimensional gradients are related to $\phi_{m,s}$ and $\chi_{m,s}$. These gradients can be defined to be consistent with (5) and (6):

$$\Psi_s = \frac{\kappa d u^*}{-B_0}(-\partial_z\Theta + \gamma_\theta) = \phi_s(\zeta)\,\chi_s(\xi), \quad (9)$$

$$\Psi_m = \frac{\kappa d u^*}{-u^{*2}}(-\partial_z|\mathbf{U}| + \gamma_u) = \phi_m(\zeta)\,\chi_m(\xi), \quad (10)$$

or they can take the traditional form, $\gamma_\theta = \gamma_u = 0$, of L19a, with $\mathbf{U}$ the Eulerian flow, not the Lagrangian. Furthermore, a justified wave parameter ξ is the fraction of the total surface layer source of TKE $P_N u^{*3}$ that is due to Stokes shear (3):

$$\xi = \frac{P_S\,\mathrm{La}^{-2}u^{*3}}{P_U u^{*3} + P_S\,\mathrm{La}^{-2}u^{*3} + P_B w^{*3}} = \frac{P_S\,\mathrm{La}^{-2}}{P_N}. \quad (11)$$

The empirical Stokes similarity functions for $\xi > 0.35$ are

$$\chi_m(\xi) = 1.03 - 2.31\,\xi + 1.58\,\xi^2, \quad (12)$$

$$\chi_s(\xi) = 0.78 - 1.20\,\xi + 0.67\,\xi^2. \quad (13)$$

In the limit of no Stokes drift ($\xi = 0$), $\chi_{m,s}$ becomes 1, so linear interpolations are taken for ξ between 0.0 and 0.35, along with constant extrapolation beyond the minimum values of

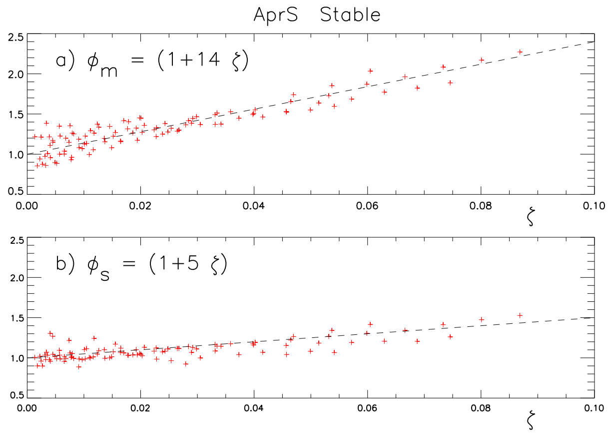

FIG. 5. Similarity functions of the stability parameter (14) calculated from hourly statistics every half hour during the stable buoyancy forcing of AprS for (a) momentum, with $\phi_m = 1 + 14\zeta$ (dashed) and (b) buoyancy, with $\phi_s = 1 + 5\zeta$ (dashed).

quadratics at $\xi = 0.73$ in (12) and $\xi = 0.89$ in (13). These minima are about 0.18 and 0.25, respectively.

In the absence of surface waves, the stability parameter is $\zeta = d/L$, where $L = u^{*3}/(\kappa B_0)$ is the Monin–Obukhov depth. In L19a surface wave effects are included in a modified depth L^*:

$$\zeta = \frac{d}{L}\left(1 + \frac{P_S}{P_U}\mathrm{La}^{-2}\right)^{-1} = \frac{d}{L^*}. \tag{14}$$

Then, calculations of $\phi_{m,s} = \Psi_{m,s}$ in the unstable surface layer of AprN and JunN, show that

$$\phi_{m,s}(\zeta) = (1 - A_{m,s}\zeta)^{-1/3}; \quad \zeta < 0, \tag{15}$$

with $A_m = 14$ and $A_s = 25$, are consistent with $\kappa = 0.4$.

Stable surface layers are only order meters thick (e.g., Fig. 3), so similar calculations of $\phi_{m,s}$ are extremely noisy, because of limited depth averaging. However, the LES TKE source integrals give ξ from (11) and hence estimates of $\chi_{m,s}$, as well as of ζ from (14), so that $\phi_{m,s} = (\Psi_{m,s}/\chi_{m,s})$ can be computed from AprS, where the Stokes forcing further reduces the noise. This exercise verifies (9) and (10) over the range $0.02 < \sigma < 0.12$. Furthermore, Fig. 5, as well as AprN despite excessive scatter, suggest the stable stability functions (dashed lines)

$$\phi_{m,s}(\zeta) = (1 + B_{m,s}\zeta); \quad \zeta > 0, \tag{16}$$

with $B_m = 14$ and $B_s = 5$, whereas both coefficients are about 5 in the atmosphere (Högström 1988). There is also an indication that Stokes forcing induces small nonlocal fluxes (negative γ_θ and γ_u), but there are other possibilities and the effects are small compared to $B_m = 14$ rather than 5. Therefore, in the absence of additional evidence, the usual assumption of $\gamma_\theta = \gamma_u = 0$, for stable boundary layers should suffice for present purposes.

4. Entrainment

A fraction of the turbulent kinetic energy produced in a boundary layer is not dissipated, but converted into column potential energy when denser water is entrained at depth then mixed throughout. An empirical rule for atmospheric convection says that the ratio of entrainment to surface buoyancy flux (B_E/B_0) is constant (Ball 1960) at about 0.2 (Tennekes 1973). An interpretation of this rule is that the integrated buoyancy source ($\langle w\theta\rangle > 0$) of TKE is proportional to w^{*3} and that a fixed fraction goes to potential energy through buoyant suppression ($\langle w\theta\rangle < 0$), whose integral over the boundary layer scales with $B_E h$. Therefore, a more general rule for ocean entrainment is formulated by empirically relating a scale for the rate of column potential energy increase to all three independent drivers of boundary layer turbulence in L19, namely, the surface layer source integrals [Eqs. (2)–(4)]. The particular scale is a robust diagnostic of buoyancy flux profiles, namely, the product of entrainment flux and depth $-B_E d_E$.

Since entrainment ($B_E < 0$) requires stable stratification near the entrainment depth, there should be a dependence on a function $F(\delta\rho)$ of a bulk density difference, $\delta\rho > 0$. For present purposes $F(\delta\rho)$ is unity, until a much greater range of ocean conditions shows how it approaches zero for an unstratified water column, and possibly increases for entrainment into the much stronger and shallower stratification of a seasonal pycnocline, for example.

If the three source integrals were equally as efficient at driving entrainment, then their combined effect would be captured by their sum $P_N u^{*3}$ from (11). This assumption is tested in Fig. 6a for AprS, JunS and D24S with Stokes shear (red), and for AprN and JunN without (blue). The linear regression (dashed) has a slope of 0.033, a small intercept and high correlation coefficient of 0.93. However, the assumption is not well justified, because of the troubling behavior near the origin. Specifically, the correlation for the 81% of instances with $-B_E d_E < 3\,\mathrm{cm}^3\,\mathrm{s}^{-3}$ falls to 0.41. Alternatively, a trivariate regression against the three TKE source integrals gives

$$(-B_E d_E) = F(\delta\rho)(0.023P_U u^{*3} + 0.038P_S \mathrm{La}^{-2} u^{*3} + 0.96P_B w^{*3}), \tag{17}$$

for $F(\delta\rho) = 1$, and neglecting a small intercept. This relationship is shown in Fig. 6b, where the behavior near the origin is much improved and the 1:1 line (dotted) is the best fit by construction. The correlation coefficient is greater than 0.96, so (17) becomes a potentially useful entrainment rule, when combined with the updated parameterizations of P_U, P_S, and P_B from section 6a.

A similar rule is developed by Li and Fox-Kemper (2017) for a widespread range of idealized LES, with steady winds, aligned waves, constant cooling, and no solar penetration:

$$(-B_E d_E) = \frac{d_E}{h}(0.17u^{*3} + 0.083\mathrm{La}_{\mathrm{SL}}^{-2}u^{*3} + 0.15w^{*3}), \tag{18}$$

where $\mathrm{La}_{\mathrm{SL}}$ is a surface layer Langmuir number, with $\mathrm{La}_{\mathrm{SL}}^2$ the ratio of u^* to the average speed of Stokes drift over the upper 20% of the boundary layer. The individual terms of (17) and (18) are not comparable, because Langmuir turbulence contributes to $\langle w\mathbf{u}\rangle$, and hence to both P_U from (2) and P_S from (3), whereas all Langmuir effects are captured by the single $\mathrm{La}_{\mathrm{SL}}^{-2}$ term of (18). Nonetheless, the two rules are comparable in

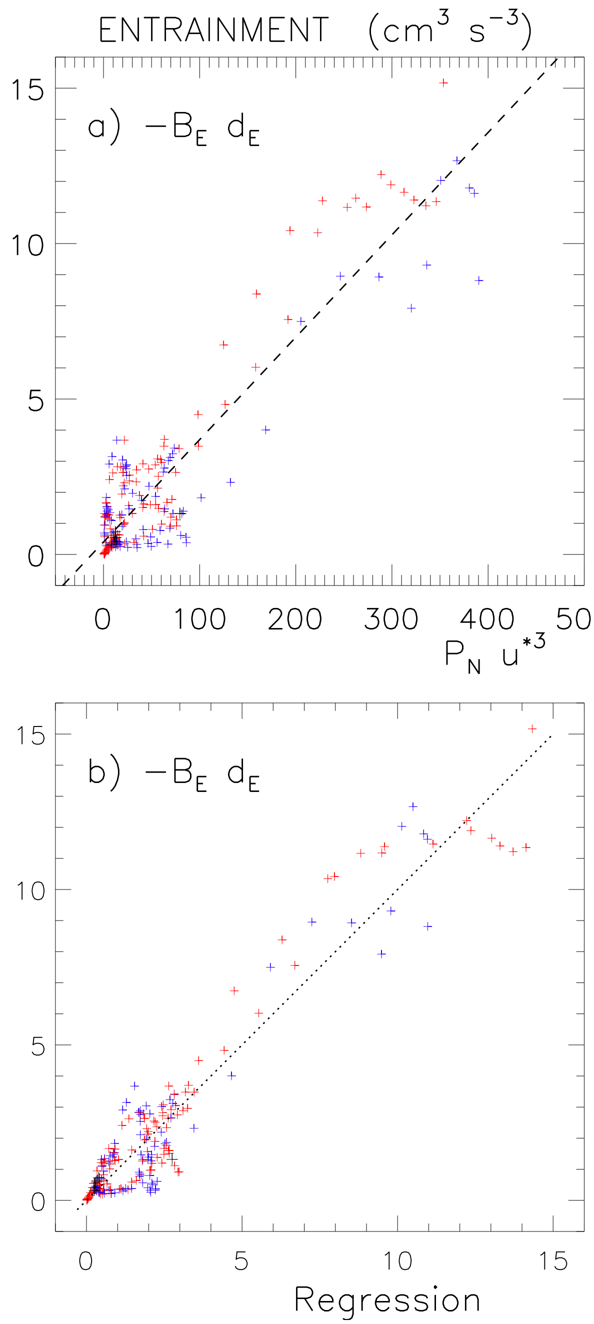

FIG. 6. The entrainment rule from independent hourly statistics showing the product $-B_E d_E$ vs (a) net surface layer production of TKE $P_N u^{*3}$, with the linear regression (dashed) and (b) calculations from the trivariate regression (17), with the best fit 1:1 line (dotted). There are 81 instances (blue) from AprN and JunN unstable buoyancy forcing plus 144 (red) more from Stokes cases, excluding the first 13 h of D24S. There are also 6 instances (black) of stable afternoon forcing from AprN and AprS.

regime E_C. With $h = h^{L19}$, they usually differ by less than 30%, and the mean bias (ratio of means) of 5% low from (18) is within the uncertainty of h, since it becomes 3% high with $h = d_E$. There are only marginal changes with the Reichl and Li (2019) dependency on La_{SL}^{-1} (e.g., lower correlation, but less bias). However, afternoon entrainment is a key to the present diurnal cycle focus, and is significantly better represented by (17). Specifically, its average over 6 h of AprN and AprS is 65% of the average $-B_E d_E$, whereas that of (18) is only 2%. The Grant and Belcher (2009) scaling, $-B_E d_E = (d_E/h^{L19})\,0.045La^{-2}u^{*3}$, applies only to the Stokes cases, when it gives a high overall correlation (0.96) and little mean bias over both entrainment regimes, but there is an order of magnitude low bias in periods such as WRW when entrainment becomes increasingly more driven by cooling ($Q_0 < 0$; $w^{*3} > 0$) relative to weakening winds and waves (Fig. 1).

A similar procedure can relate any measure of entrainment to the source integrals over different depth ranges. For example, M_E, the integral of (4) over the entrainment zone of $\langle w\theta \rangle < 0$, gives the rate of conversion of TKE to potential energy across the zone. It is the basis for determining the all-important boundary layer depth in the ePBL scheme of Reichl and Hallberg (2018) and its extension to Langmuir turbulence by Reichl and Li (2019). Its correlation coefficient with $P_N u^{*3}$ is 0.71, which with a trivariate regression increases to 0.85, but the fit near the origin, including a high afternoon entrainment bias, is not much improved. When input into the Reichl and Li (2019) empirical relation, M_E is an excellent predictor of B_E in regime E_C (0.98 correlation; 3% low bias). However, in regime E_W there is more than a factor of 2 high mean bias, despite high values of ($-B_E/|B_0| > 1$), because $-M_E$ integrals are relatively even higher as a consequence of the entrainment zone extending from the surface to more than twice the entrainment depth in Fig. 3d, for example. Also contributing are the highly nonlinear buoyancy flux profiles that appear to be a consequence of prior conditions. Nonetheless, this approach appears to be viable at least for regime E_C where the profiles are more linear and the ePBL assumption that the depth of neutral stratification bounds the entrainment zone could be modified to account for the 20 m difference in Fig. 3a, for example. In regime E_W the relatively high values of $-B_E$ are largely compensated by smaller entrainment depths in the $-B_E d_E$ product of Fig. 6 and (17).

Another application of the procedure relates $-B_E d_E$ to the source integrals above $-h^{L19}$, $-d_E$, or $-d_i$. With any of these limits, the resulting regression coefficients corresponding to those of (17) become 0.020, 0.035, and 0.27. Respectively, these values are the fractions of TKE produced by Eulerian shear, Stokes shear, and buoyancy that go to increasing potential energy rather than dissipating. Buoyancy is by far the most efficient with over 25% going to entrainment, and so contributes about 10% of the regime E_C driving of AprS before the winds weaken at hour 15, and as much as 90% afterward, but is negligible in regime E_W. Although much less efficient, the Stokes source usually contributes more than 70% of the entrainment driving, except for the WRW period. The largest Eulerian shear contribution of AprS is only about 20% in regime E_W.

a. *Entraining boundary layer depth*

An entraining boundary layer has a unique depth h^{BL}, where the entrainment flux, $B_E < 0$, equals the buoyancy flux from

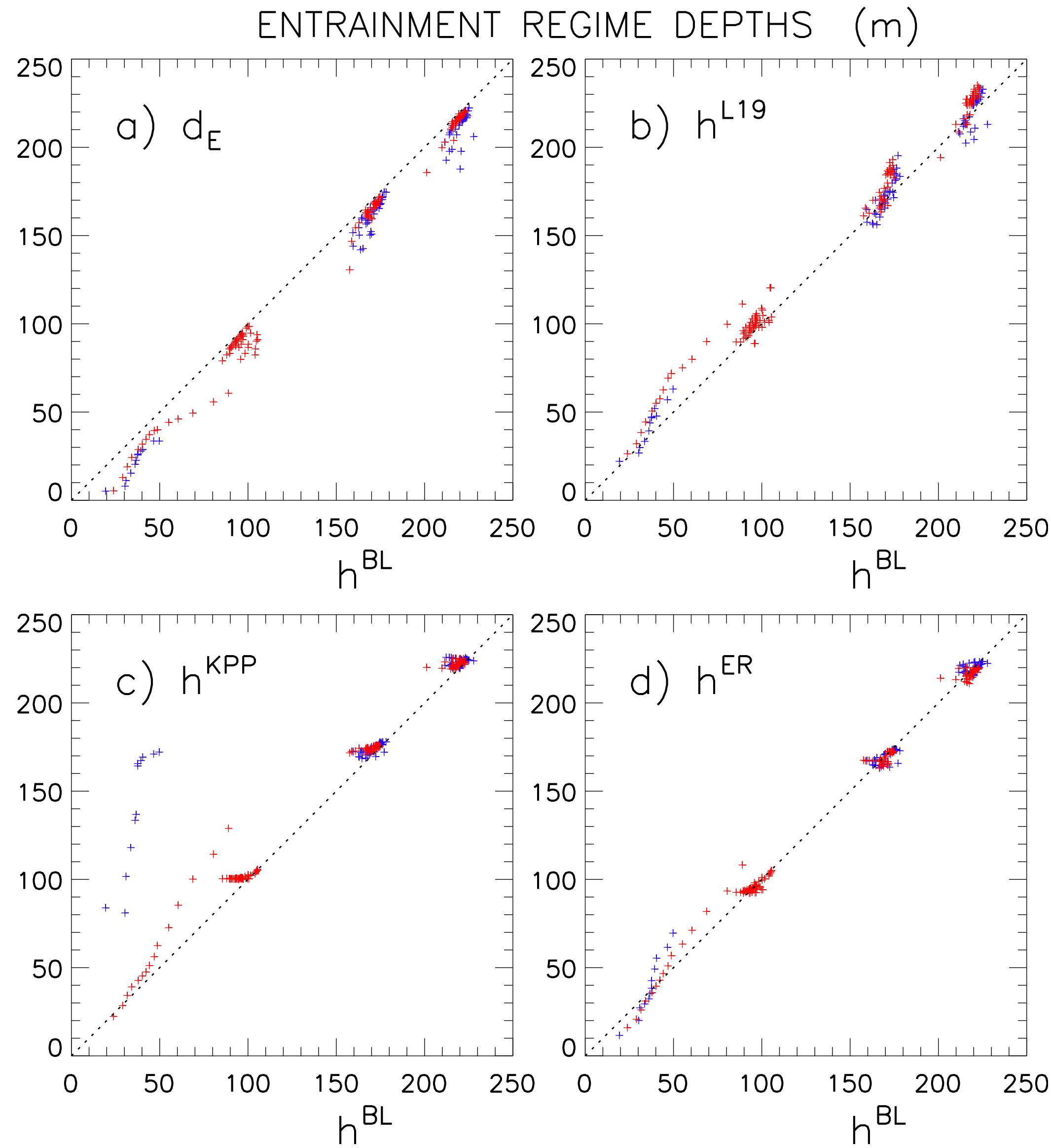

FIG. 7. Comparison of the boundary layer depth h^{BL} to other Table 1 depths diagnosed from 224 independent hourly statistics throughout the entrainment regimes of AprS, JunS, and D24S with Stokes forcing (red) and from AprN and JunN (blue): (a) entrainment depth d_E, (b) h^{L19}, (c) the KPP boundary layer depth of Danabasoglu et al. (2006), and (d) parameterized h^{ER} from the entrainment rule (section 6).

(5), given the diffusivity of (7), and Γ_θ from (8). It is the first depth below d_E, where

$$B_E = G_C(\sigma_E)\left[\frac{\kappa u* h^{BL}\,\partial_z\Theta(d_E)}{\phi_s(\zeta)\,\chi_s(\xi)} - R_s\frac{(|B_0| - B_0)}{2}\right], \qquad (19)$$

but limited to $\sigma_E = (d_E/h^{BL}) > 0.225$, where G_C is maximum (Fig. 4). Figure 7b compares the boundary layer depths, h^{BL} and h^{L19} from all the entrainment regimes of cases with Stokes forcing (red) and without (blue). Depths around 220 m are from June, those from D24S are near 100 m, and the others are from April. Each cluster displays more spread in h^{L19}, which Fig. 2 indicates is due to hourly variability not reflected in either TKE, or $\langle w\theta\rangle$. Therefore, there has been no attempt to parameterize h^{L19}. However, the entrainment rule (17) allows h^{BL} to be parameterized as h^{ER} in section 6, so it is the preferred choice, and compared to other depths (Table 1) in Fig. 7. It is less than 10 m deeper than d_E (Fig. 7a), except in regime E_W of AprS as it increases from 50 to 100 m, and also when d_E is less than about 15 m following the transition from regime SBL.

Figure 7c compares the KPP boundary layer depth calculation, h^{KPP}, as updated in Danabasoglu et al. (2006). The major differences are during regime E_W when h^{KPP} becomes greater than $h^{L19} > h^{BL}$, because it is less affected by the weak diurnal stratification near d_i^* (Fig. 3c). These differences and the general deep bias of h^{KPP} would increase with the Li and Fox-Kemper (2017) modifications to incorporate the effects of Langmuir turbulence. Also in regime E_W, h^{KPP} is shallower in AprS than AprN, but not if the calculation uses Lagrangian shear instead of just the Eulerian, which is much reduced by Stokes forcing.

b. Flux profiles during entrainment

The defining characteristic of the entrainment regimes is buoyancy loss ($\partial_z\langle w\theta\rangle > 0$) between the surface and the entrainment depth, with gain below to beyond the boundary layer depth. Buoyancy loss through the surface ($B_0 < 0$) is usual (Fig. 3a), but not necessary (Fig. 3d). Furthermore, the buoyancy flux varies smoothly with depth, as also seen in Fig. 8 (upper panels; solid profiles). Positive curvature across the boundary layer is a singular feature of regime E_W, when the diurnal stratification weakens, and its local maximum deepens steadily from $d_i^* = 15$ to 80 m (Fig. 2), but it is not eroded away. The effect of using the quadratic, G_C, of Fig. 4, rather than G_C^{L19}, is to deepen h^{BL}, but even so it tends to be shallower than h^{L19}. Therefore, the buoyancy flux at h^{BL} can be significantly negative (e.g., Fig. 8).

Figure 8 also shows the magnitude τ of the turbulent stress and momentum flux (middle panels; solid blue profiles) decreasing monotonically from u^{*2} at the surface to relatively small values at h^{BL}, except over the WRW period. At hour 26, for example, the profile remains smooth, but its negative curvature suggests a depth-dependent delay in the response to the varying wind. A similar response is evident in the June MRW period. Thus, these two periods of counterinertial wind rotation are not typical of regime E_C, but will be designated as such until it can be determined how relevant parameters, such as the depth of maximum τ ($\approx$70 m at hour 26), depend on the wind's time history.

The Eulerian shear vector $\partial_z\mathbf{U}$ is typically a small difference between much larger horizontal velocities, so its orientation is highly sensitive to the relative influence of wind and waves on the momentum flux vector, and to any differential Coriolis acceleration. Therefore, relative to this shear the angles of the stress Ω and of the wind Ω_W (Table 1) can have a complicated vertical structure. The free slip boundary condition aligns the stress and shear vectors with the wind, $\Omega = \Omega_W = 0$, only at the surface. As the shear veers with depth, the stress stays more aligned with the wind, so its angle relative to the wind vector, $\Omega_\tau = \Omega - \Omega_W$, diverges from the angle of the shear from the wind, $-\Omega_W$. The angle Ω_τ is almost always in an inertial sense (positive in the Southern Hemisphere) and increases steadily with depth, as shown in Fig. 8 (bottom panels; solid dark blue). This angle should be related to orientations of the shear relative to the wind at multiple scales. A simple, yet effective, representation of the large scale is the angle Ω_L^{LS} of the Lagrangian velocity difference from the near surface. In practice, the near surface value is the sum of the uppermost LES Eulerian velocity and the average Stokes drift down to where its speed becomes less than $0.9\mathrm{La}^{-2}u^*$. The small scale is similarly represented by a single angle Ω_E^{SS}, of the local Eulerian velocity difference over about five meters depth, provided this angle is between $-\pi/4$ and $3\pi/4$. Angles outside this range are linearly downweighted and not used if less than $-\pi/2$, or greater than $5\pi/4$.

Bivariate regressions from 25 roughly evenly space depths in the boundary layer give correlation coefficients of 0.80 from all cases, 0.90 from AprS, and 0.86 over the three Stokes cases, so there is potentially a little to be gained by increasing the number of vertical scales and perhaps higher-order velocity differences. Neglecting a small intercept, the Stokes cases give a parameterization of Ω_τ in the boundary layer, namely,

$$\Omega_\tau^{\mathrm{BL}} = 0.35\,\Omega_E^{\mathrm{SS}} + 2.3\,\Omega_L^{\mathrm{LS}}; \tag{20}$$

The results from AprN and JunN are indistinguishable, but not if the Stokes drift is included in Ω_E^{SS}. Profiles of $\Omega_\tau^{\mathrm{BL}}$ are shown in Fig. 8 (bottom panels; dashed blue). Their high degree of agreement with Ω_τ (solid blue) across regimes, makes formulating the momentum flux as a magnitude and direction relative to the wind an attractive option. However, the Fig. 8 differences between $-\Omega_W$ (solid red) and Ω_τ demonstrate that the common assumption of stress and shear alignment is not generally valid. The dramatic swings of $-\Omega_W$ over the upper 20 m appear to be due to Stokes effects, because they are also evident in D24S and to a lesser extent in JunS, but in neither AprN, nor JunN. In the WRW example, the stress vector is oriented more than 180° in an inertial sense from the shear vector between about 5 and 70 m, yet $\Omega_\tau^{\mathrm{BL}}$ remains representative.

5. The stable boundary layer and detrainment

Figure 9 shows time histories of various depths (Table 1) that bound the zones and layers of AprS (red) and AprN (blue) during the single day of stable buoyancy forcing. These depths are shown along with the profiles of $\langle w\theta\rangle$, τ and Ω_τ in the four examples of Fig. 10. The boundary layer depth of choice, h, is shown in Fig. 9a (solid traces). It follows h^{BL} when the buoyancy forcing is unstable, and the depth, h^{AM} (Fig. 9c), of a growing morning boundary layer from the unstable to stable transition at t_{US} in regime DBL until the reverse transition at t_{SU} in regime E_W.

The boundary layer depth h^{L19} of Fig. 9b is always available (Fig. 2). However, a depth where the integrated Lagrangian shear production of TKE balances the buoyant suppression (gray triangles) can be found only between hours 34 and 37. In stable atmospheric boundary layers, this depth has been associated with the Monin–Obukhov depth (Wyngaard 2010), which appears to be the case near hour 35 of AprS for κL^* (gray trace), as defined by (14).

An unusual characteristic of the stable regimes is a shallow depth d_{MKE}, where the flow speed, and hence the mean kinetic energy, are at minima. Figure 9c shows this depth increasing throughout the day and into the night. It provides a bound on h, because dominant surface forcing would maintain $\partial_z|\mathbf{U}|^2 > 0$. Throughout regimes DBL and SBL, h^{L19} (Fig. 9b) does not remain within the d_{MKE} bound and, therefore, is not a viable boundary layer depth. However, assuming internal morning

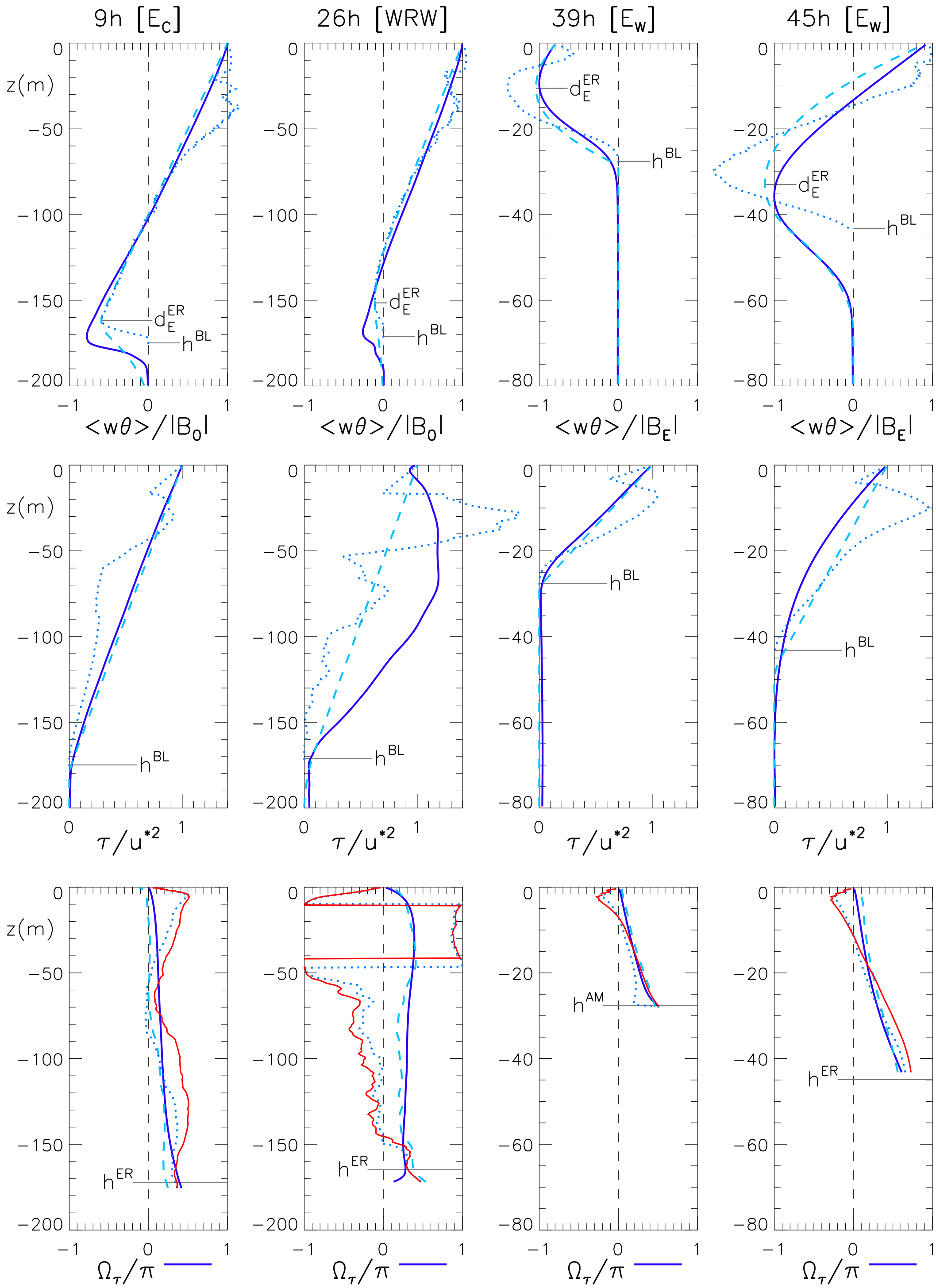

FIG. 8. Vertical profiles during the entrainment regimes E_C (hours 9 and 26), and E_W (hours 39 and 44) from AprS: (top) buoyancy flux normalized by the greater of $|B_0|$ or $|B_E|$ (solid blue), and the parameterizations from section 6, $\langle w\theta\rangle^{FP}$ (dashed) and $\langle w\theta\rangle^{KP}$ (dotted); (middle) stress magnitude normalized by u^{*2} (solid blue) and the parameterizations, τ^{FP} (dashed) and τ^{KP} (dotted); and (bottom) vector orientations from the wind of the shear $-\Omega_W$ (red profiles) and of the stress Ω_τ (solid blue) and its parameterizations $\Omega_\tau^{FP} = \Omega_\tau^{BL}$ (dashed) from (20) and Ω_τ^{KP} (dotted) from section 6a. The parameterized depths (Table 1) are h^{AM} from (21), and from section 6, d_E^{ER} and h^{ER} are consistent with (17).

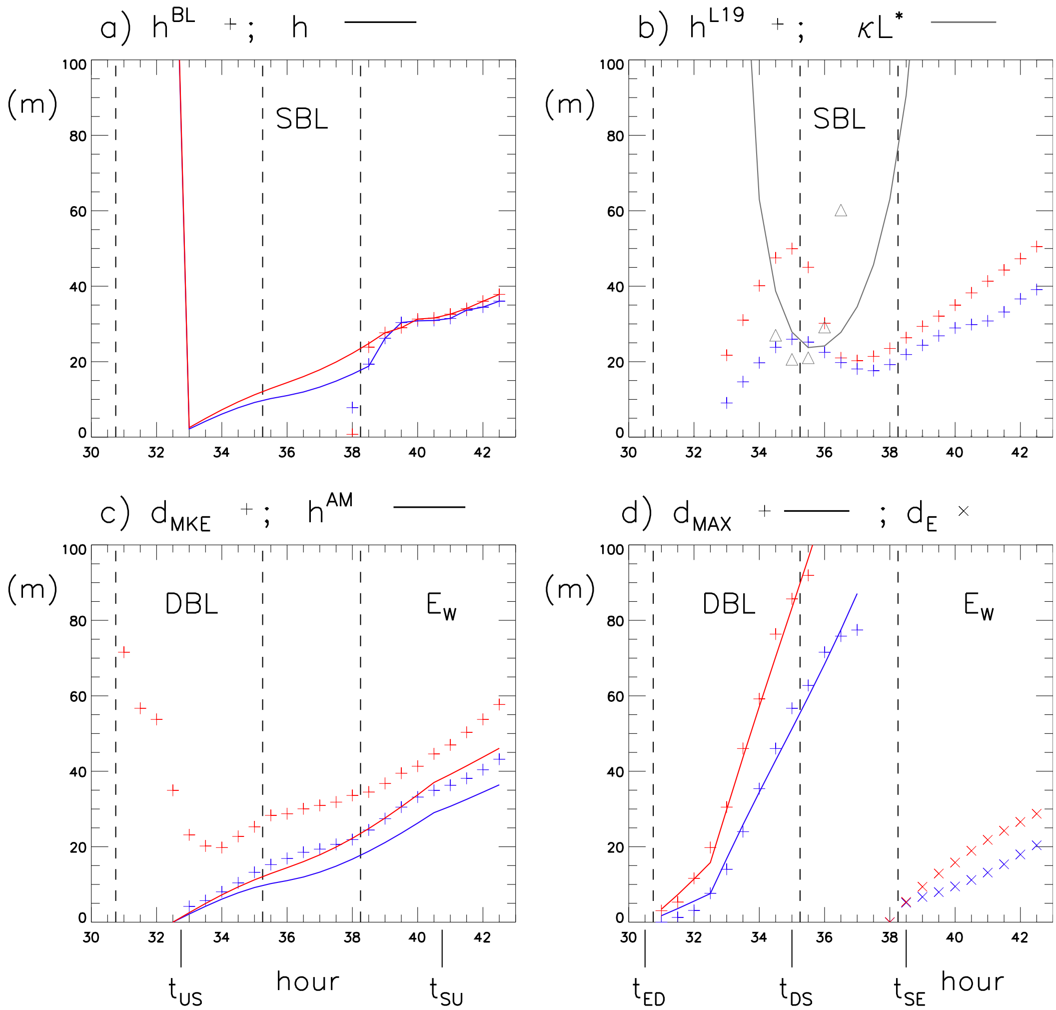

FIG. 9. Half-hourly time variability of diagnostic and time-integrated depths (Table 1) from hourly statistics of AprS (red) and AprN (blue) during regimes DBL, SBL, and E_W: (a) h^{BL} and the boundary layer depth of choice, h (solid traces); (b) h^{L19} and κL^* (gray trace) from (14), as well as the AprS depths (gray triangles) at which the Lagrangian shear production of TKE is balanced by buoyant suppression; (c) d_{MKE} and the depth of the morning boundary layer, h^{AM} (solid traces) from (21); and (d) depth of the maximum positive buoyancy flux d_{MAX}, both as diagnosed (symbols) and as integrated from (22), and the afternoon entrainment depth d_E. The vertical dashed lines mark the regime transitions, near times t_{ED} (E_C to DBL), t_{DS} (DBL to SBL), and t_{SE} (SBL to E_W). The transition from unstable to stable buoyancy forcing is shown at t_{US} and from stable to unstable at t_{SU}.

boundary layers grow at a rate proportional to the wind and wave forcing, tempered by buoyancy, leads to

$$\partial_t h^{AM} = (0.025u^{*3} + 0.00015\mathrm{La}^{-2}u^{*3} - 0.0015B_0 h^{AM})^{1/3}, \tag{21}$$

where the empirical coefficients are chosen so that h^{AM} in Fig. 9c (solid traces) remains less than d_{MKE} (symbols) and matches both h^{BL} and h^{L19} during regime E_W, for both AprS and AprN. These criteria are also satisfied throughout regime SBL by $\kappa L^*(t_{DS})$ at the transition from regime DBL. Furthermore, the vertical flux profiles of Fig. 10 reflect a depth close to both these depths in the SBL example, but not during detrainment when there is no signature of any boundary layer depth. The validity of (21) over the full range of diurnal cycles has not yet been established. Therefore, a more robust regime SBL option may prove to be $h = \kappa L^*(t_{DS})$ until afternoon entrainment in regime E_W allows h^{BL} and h^{ER} to be calculated.

a. Detrainment

Following section 2, Fig. 9d shows the depth d_{MAX} of maximum buoyancy flux, $B_{MAX} > 0$, during detrainment. Its appearance marks the transition to regime DBL at $t_{ED} = 30.75$ h. Such a maximum remains clearly discernible at hour 34 in Fig. 10, but not in regime SBL. In the detrainment examples of Fig. 10 (top panels), d_{MAX} separates buoyancy gain from the loss down to near $d_E(t_{ED})$, the entrainment depth at t_{ED}. In contrast, the corresponding stress profiles (middle panels) do

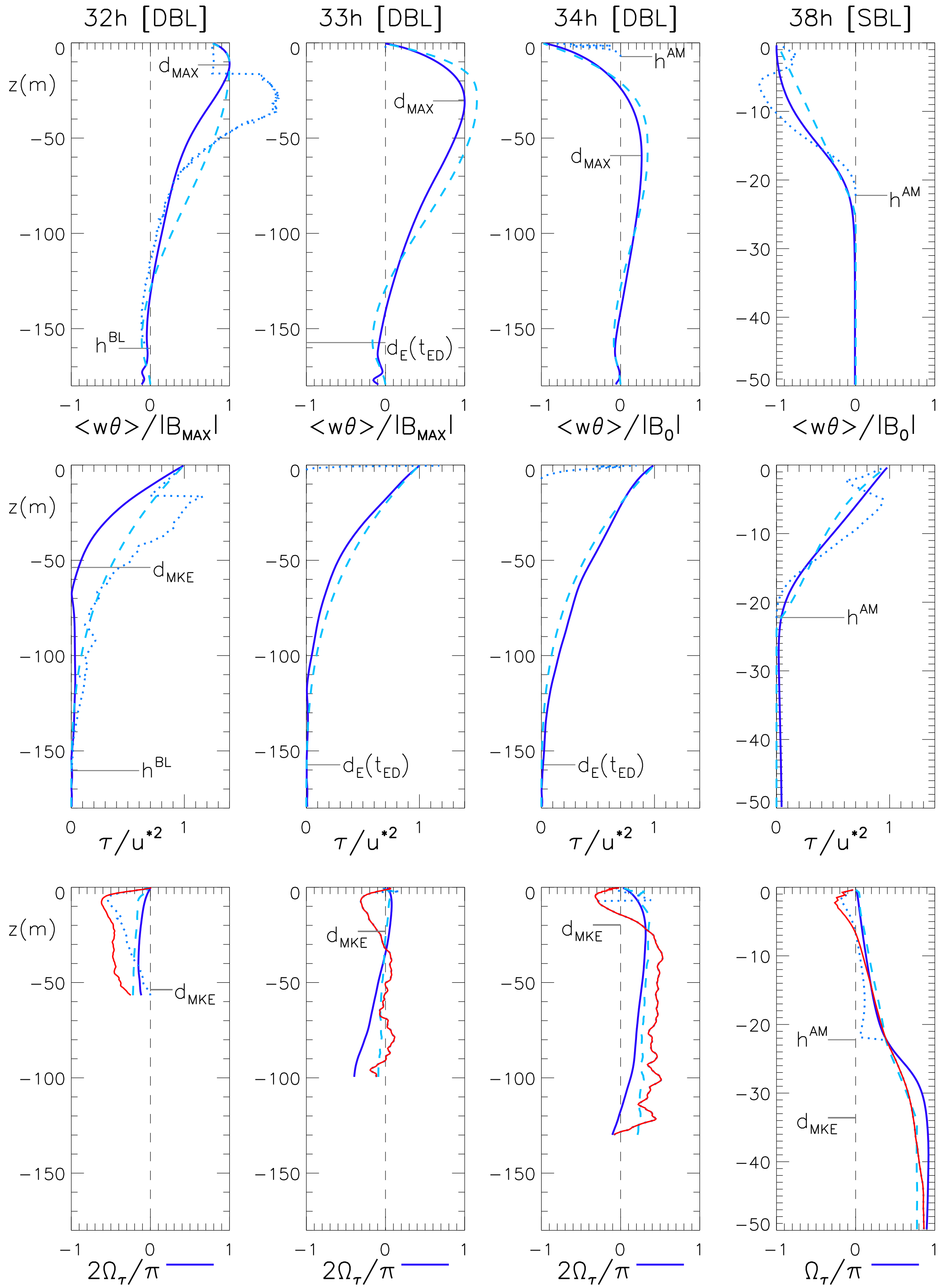

FIG. 10. As in Fig. 8, but for the detrainment regime DBL (hours 32, 33, and 34), with Ω_τ^{DZ} (dashed blue) from (24) below 2 m, and for the stable regime SBL (hour 38), with Ω_τ^{DZ} below d_{MKE}. Also, the buoyancy flux is normalized with the greater of $|B_0|$ or $|B_{max}|$ and angles are shown only for $\tau > 0.05u^{*2}$.

not appear to reflect d_{MAX}, but decrease monotonically from u^{*2} at the surface and approach zero near either d_{MKE} (hour 32), or $d_E(t_{\text{ED}})$ at hours 33 and 34, or h_{AM} (regime SBL).

In Fig. 9d, d_{MAX} deepens more rapidly during the stable hours of regime DBL than the unstable, and with Stokes forcing than without. Following (21), this behavior is captured (solid traces) by integrating

$$\partial_t d_{\text{MAX}} = (a_1 u^{*3} + a_2 \text{La}^{-2} u^{*3})^{1/3}, \tag{22}$$

starting at t_{ED}, with empirical coefficients $a_1 = a_2 = 0.002$ until t_{US}, and $a_1 = 0.20$, $a_2 = 0.05$ afterward, for both AprS and AprN. If turbulence remained steady after t_{ED}, then B_{MAX} would be the buoyancy flux at d_{MAX} at time t_{ED}. However, turbulent transport and dissipation are two processes of change. The vertical structure of Fig. 2b, suggests that transport enhances the near surface buoyancy flux, and assuming that it does not change the integral (4) above the entrainment zone, and that the profile at t_{ED} is linear from $-B_0$ at the surface to $f_B B_0$ at d_E, gives a detrainment rule, akin to the entrainment rule (17), but involving prior forcing and d_{MAX} from (22):

$$B_{\text{MAX}}^{\text{PAR}} = B_0(t_{\text{ED}})\left[f_E - \frac{d_{\text{MAX}}}{d_E(t_{\text{ED}})}(2f_E - 1)(1 + f_B)\right], \tag{23}$$

where $f_E = 1.15$ is the effective near surface enhancement. A simple means of accounting for turbulent dissipation and its reduction of B_{MAX} to zero is with $f_B = 0.5$; more than $-B_E/B_0$ at t_{ED}, but less than at hour 9 (Fig. 8), for example. The comparison of Fig. 11a shows that (23) then represents the early decrease of B_{MAX} from near B_0 (t_{ED}) and its later approach to zero, during regime DBL of both AprS (red) and AprN (blue). This general behavior is captured also during regime DBL of JunS (black), but is sensitive to when the integration of (22) begins at t_{ED}.

In Fig. 10 (bottom panels), the stress direction from the wind Ω_τ (solid blue) is tracked by Ω_τ^{BL} only to about 2-m depth in regime DBL, and to $h = h^{\text{AM}}$ during regime SBL. However, a consequence of $\partial_z|\mathbf{U}|$ changing sign at d_{MKE} is a nearby change in the sign of Ω, which is reflected in a detrainment zone parameterization of Ω_τ,

$$\Omega_\tau^{\text{DZ}} = \Omega_W + \tan^{-1}\frac{\partial_z|\mathbf{U}|}{|\partial_z \mathbf{U}|} + 10°, \tag{24}$$

where the 10° constant is a consequence of the slightly different depths of the sign changes. In the regime DBL examples of Fig. 10, Ω_τ^{DZ} (dashed blue) tracks Ω_τ across all depths below 2 m. Thus, Ω_τ^{DZ} follows neither the increase in Ω (solid blue–red) to a maximum at about 5 m, nor its decrease to near zero at d_{MKE}. Below d_{MKE} in both regimes DBL and SBL, the stress orientation is better represented by Ω_τ^{DZ} than by the shear direction, at least until τ falls below about 0.05 u^{*2}. In regime SBL, a weighted average of Ω_τ^{BL} at h^{AM} and Ω_τ^{DZ} is used to give a smooth transition between h^{AM} and d_{MKE}.

In Fig. 2a, the turbulent kinetic energy in the detrainment zone between $h = h^{\text{AM}}$ and $d_E(t_{\text{ED}})$ decreases smoothly with both depth and time and by t_{DS} it is nearly uniform at about $u^{*2} = 0.8\text{cm}^2\,\text{s}^{-2}$. Thus, TKE behavior does not display the depth–time dependencies of either the buoyancy flux (Fig. 2b), or the stress vector. In particular, it reflects neither d_{MAX}, nor d_{MKE}.

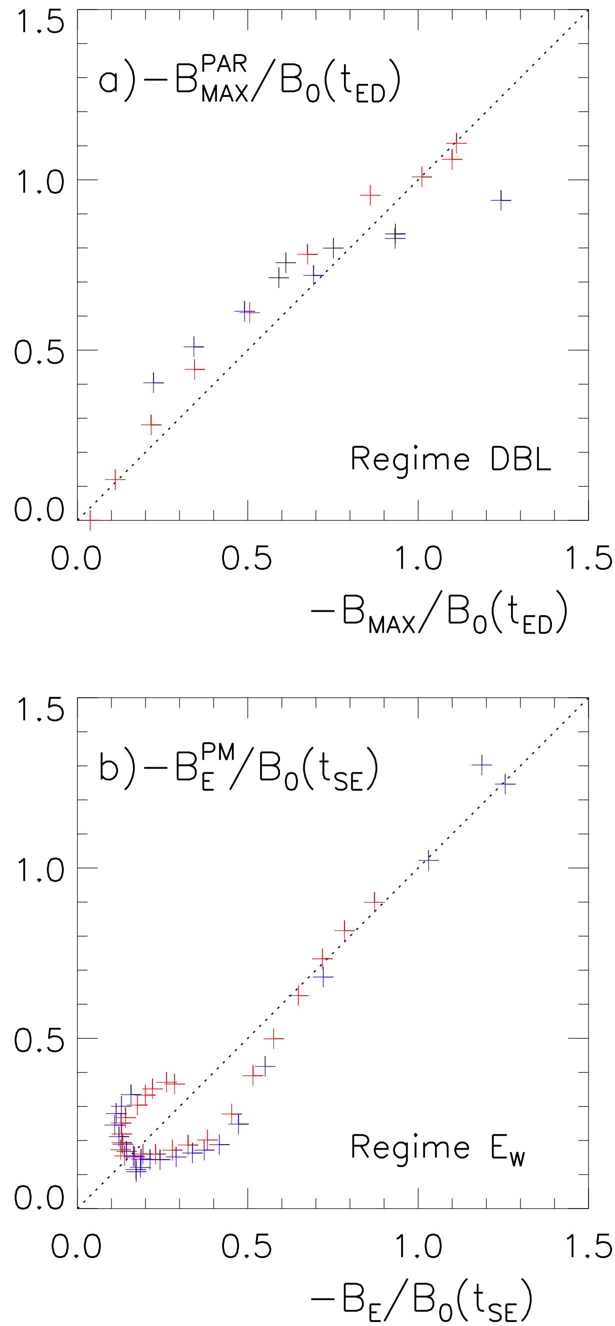

FIG. 11. Evaluation of the rules for regime DBL detrainment and for regime E_W afternoon and nighttime entrainment from AprS (red) and AprN (blue) and from JunN and JunS (black): (a) $B_{\text{MAX}}^{\text{PAR}} > 0$ from (23) vs B_{MAX}, normalized by $B_0 < 0$ at the time $t = t_{\text{ED}}$ of transition to regime DBL and (b) $B_E^{\text{PM}} < 0$ from (32) vs B_E, normalized by $B_0 > 0$ at time $t = t_{\text{SE}}$ of transition to afternoon entrainment. Values are calculated half-hourly from hourly statistics.

6. Empirical turbulence models of the diurnal cycle

The vertical fluxes of buoyancy and momentum are parameterized in terms of the ocean state, surface fluxes and Stokes drift in two distinct ways. The first ETM (K-profile) is based on diffusivity and viscosity in the boundary layer. In the detrainment zone, for example, the rules from section 5a are formulated as analytic profiles of buoyancy flux and stress magnitude, along with Ω_τ^{DZ}. The second approach (F-profile) extends this concept to all regimes by utilizing Ω_τ^{BL}. In principle, the ocean state from either observations or an OGCM could give the stratification and the shear, but evaluation is compromised by the lack of direct flux measurements, and forcing error. Therefore, as practical first step, both schemes are evaluated directly against LES fluxes from the wide range of conditions represented by AprS, JunS, and D24S with Stokes forcing and AprN and JunN without, by taking the ocean state and forcing from each case. Thus, numerical sensitivities to grid resolution and time step in the van Roekel et al. (2018) evaluation of KPP, for example, are avoided. The distributions of the vertical fluxes of buoyancy, downwind momentum and crosswind momentum are compared visually and statistically. In L19a, nonzero across-shear momentum flux Γ_v (6) directly shows the error associated with the common assumption of downgradient viscosity, but its distribution is not shown here, because further interpretation is hampered by a coordinate that rotates with depth.

a. K-profile (KP) boundary layer fluxes

The first approach is akin to the KPP scheme of Large et al. (1994), except Stokes forcing from L19 is included, there is an across-shear momentum flux given by Γ_v from (8) and the boundary layer depth differs (Fig. 7c). In addition, the composite shape function (Fig. 4) and the nondimensional gradients (9) and (10) simplify the KP fluxes in the surface layer ($\sigma < \varepsilon$) to

$$\langle w\theta\rangle^{KP} = -B_0\frac{G_C(\sigma)}{\sigma} + \Gamma_\theta\,; \qquad \tau^{KP} = u^{*2}\frac{G_C(\sigma)}{\sigma}\,, \tag{25}$$

with $\Omega^{KP} = \sin^{-1}(-\Gamma_v/\tau^{KP})$, so that as (G_C/σ) converges to 1 at the surface the boundary conditions ($\langle w\theta\rangle = -B_0; \tau = u^{*2}; \Omega = 0$) are satisfied. Below the surface layer ($\varepsilon < \sigma < 1$), G_C as defined by (7) relates the vertical fluxes and gradients of (5) and (6):

$$\langle w\theta\rangle^{KP} = w_s^{PAR}h^{PAR}G_C(-\partial_z\Theta) + \Gamma_\theta + B_h^{PAR}H(d), \tag{26}$$

$$\begin{aligned}\langle wu\rangle^{KP} &= w_m^{PAR}h^{PAR}G_C(-\partial_z U + \gamma_u) + \tau_h^{PAR}H(d)\\ &= -\tau^{KP}\cos\Omega^{KP},\end{aligned} \tag{27}$$

$$\langle wv\rangle^{KP} = \Gamma_v = -\tau^{KP}\sin\Omega^{KP}, \tag{28}$$

where Γ_θ and Γ_v are given by (8), and $\gamma_u = 0$ (section 3). Furthermore, nonzero fluxes at a parameterized boundary layer depth h^{PAR} are themselves parameterized as downgradient fluxes by specifying local eddy transfer coefficients $v_{m,s}$:

$$B_h^{PAR} = -v_s\,\partial_z\Theta(h^{PAR})\,; \qquad \tau_h^{PAR} = -v_m\,\partial_z U(h^{PAR})\,. \tag{29}$$

These fluxes are assumed to be driven from the interior and to diminish according to a specified function $H(d)$, which for present convenience decreases linearly from unity at h^{PAR} to zero at d_E and at $1.2h^{PAR}$.

Following section 3, parameterized TKE source integrals are required to compute ζ from (14) and ξ from (11) and hence $\chi_{m,s}^{PAR}$ and $\phi_{m,s}^{PAR}$ and finally the turbulent velocity scales in (26) and (27), as defined by (7): $w_{m,s}^{PAR} = \kappa u^* h^{PAR}(\chi_{m,s}^{PAR}\,\phi_{m,s}^{PAR})^{-1}$. However, the parameterizations developed in L19 are based on integrals from $-\varepsilon h^{L19}$ to the center of the topmost LES grid cell. Therefore, there are slight modifications here for the different integration limits ($-\varepsilon h$ to 0) and for the exclusion of sinks of TKE in (2), (3), and (4), namely, the coefficients of (8), (12), and (13) as well as $P_B^{PAR} = 0.094$ for unstable buoyancy forcing, or zero for stable. In addition, $\Omega^{PAR} = (\Omega_\tau^{BL} + \Omega_W)$ from (20) leads to much improved and simpler parameterizations of P_U and P_S, and hence of the turbulent velocity scales. For example, assuming a linear decrease of τ from the surface wind stress to zero at h^{PAR}, as seen in Fig. 8, allows the integrand of (2) to be approximated, such that TKE sources ($\cos\Omega^{PAR} > 0$) give

$$P_U^{PAR}u^{*3} = \int_{-\varepsilon h^{PAR}}^{0}\left[u^{*2}\left(1+\frac{z}{h^{PAR}}\right)|\partial_z\mathbf{U}|\cos\Omega^{PAR}\right]dz\,. \tag{30}$$

A similar exercise using the angle between the stress and Stokes shear vectors improves P_S^{PAR}, especially over the WRW period, when depths where the cosine of this angle is negative are again excluded from the integrals.

These two new parameterizations are evaluated in Fig. 12. Despite differences between h^{BL} and h^{ER} (Fig. 7d), the 1:1 lines (dotted) are good fits to cases with Stokes drift (red) and without (blue) over the entire range, though there is somewhat more spread of the black symbols from the WRW period in April and the MRW in June. Nevertheless, all the points of Fig. 12 give correlations of 0.99 for both P_U^{PAR} (229 instances) and P_S^{PAR} (143 instances), small mean biases (<3%) and no alarming outliers. The higher Fig. 12a values from AprN and JunN (blue) reflect the much greater Eulerian shear. Unlike L19a, this variability is now well represented by (30), as are the lower P_U values from shallow stable boundary layers, both with and without Stokes drift. The more consistent behavior when TKE sinks are excluded suggests that the associated energy loss is largely compensated by reduced dissipation, rather than by weaker entrainment.

The K-profile fluxes also depend on a depth scale such as a boundary layer, or entrainment depth. A very simple approach would be to use the MLD as defined by de Boyer Montégut (2004) as the depth where the density (buoyancy) difference from the surface first exceeds a $0.03\,\mathrm{kg\,m^{-3}}$ threshold. However, this depth remains nearly constant at about 172 m throughout all regimes of AprS. A much smaller threshold is needed to detect the diurnal cycle. For example, with $0.006\,\mathrm{kg\,m^{-3}}$, the modified MLD* shown in Fig. 13c does shoal to 20 m, but not until hour 37, and by hour 41 it is already deeper than 150 m.

The alternative, h^{PAR}, is adapted from sections 4a and 5. Whenever the buoyancy forcing is unstable, the shallowest depth h^{ER} is found where a shallower depth d_E^{ER} and entrainment flux B_E^{ER} computed from (26), are consistent with the entrainment rule (17). In Fig. 7d, there are no significant systematic differences between h^{BL} and h^{ER} over the unstable

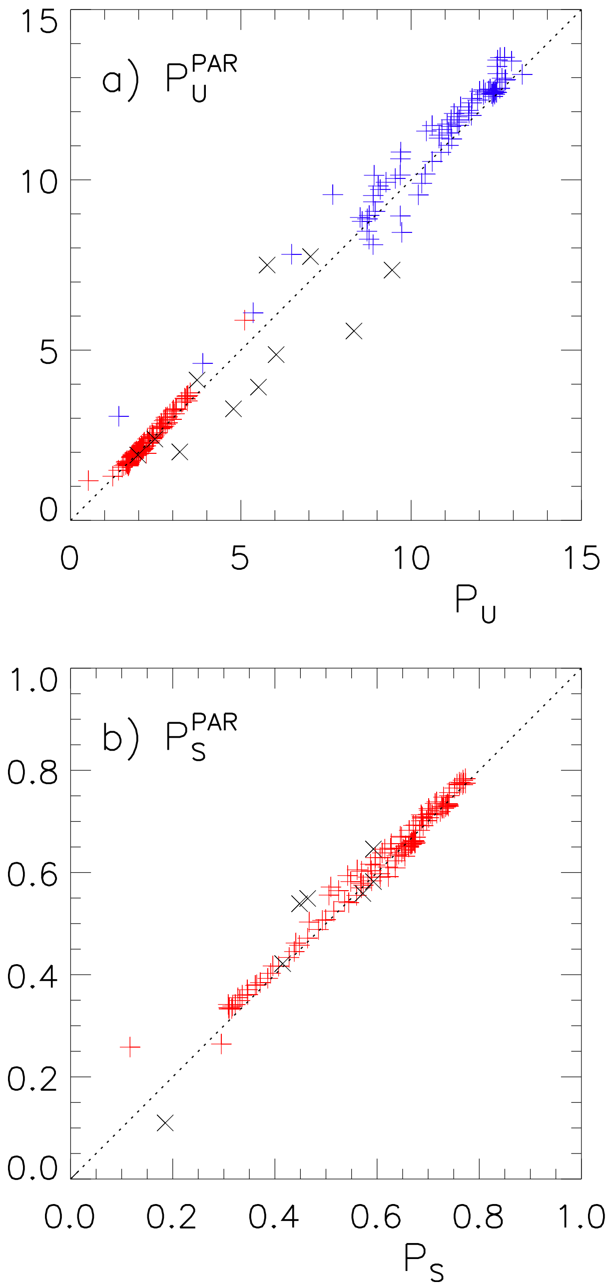

FIG. 12. Evaluation of the parameterizations of the surface layer TKE production integrals, $P_U^{PAR}u^{*3}$ and $P_S^{PAR}\mathrm{La}^{-2}u^{*3}$ from all three Stokes cases (red) and from AprN and JunN (blue), except the black symbols are from the April WRW and June MRW periods.

entrainment regimes, though h^{BL} has about twice the spread. With stable forcing h^{PAR} equals h^{AM} shown in (Fig. 9) from integrating (21). Thus, h^{PAR} varies more smoothly in time (Figs. 13b,c) than either h^{BL} (Fig. 13a) or h^{L19} (Fig. 2).

Figures 8 and 10 also show K-profile fluxes (dotted blue) throughout the boundary layer, with $v_{m,s} = 0$ in (29) convenient for the purpose of revealing major problems above the entrainment depth. Perhaps the most prevalent (bottom panels) is that during entrainment $\Omega^{KP} = \tan^{-1}(\langle wv\rangle^{KP}/\langle wu\rangle^{KP})$ tracks the near surface veering of the shear, such that Ω_τ^{KP} (dotted blue) tracks $(-\Omega_W)$ (red) and deviates radically from Ω_τ (solid blue), though there is often better agreement at depth. Also, the entrainment is too vigorous throughout regime E_W (e.g., by about 40% at hour 39). In addition, the positive bias in τ^{KP} between 20- and 60-m depth over the WRW period and into regime DBL, suggests that the shear, stress and variable forcing are far from equilibrium. Finally, K-profile fluxes in the detrainment examples of Fig. 10 are not faithful representations in the boundary layer and are missing below, even though they display considerable fidelity below 40 m at hour 32. Perhaps less serious issues include discontinuities at $d = \varepsilon h^{PAR}$, as well as the fluxes at h^{PAR}. A possible approach to the former would be to blend the surface layer fluxes from (25) over a range of depths, and the latter could be overcome by tuning the function $H(d)$ and the values of $v_{m,s}$ in (29). However, such solutions may not be universally applicable.

b. F-profile (FP) parameterizations

To utilize h^{AM} and to address detrainment and afternoon entrainment, the appropriate regimes (section 2b) need to be identified without knowledge of the buoyancy flux, especially DBL and E_W that are most problematic for K-profile. For this purpose the key factors are the meteorological forcing (Fig. 1); the Langmuir number, La; the Monin–Obukhov depth L; the local maximum stratification at d_i^* (Fig. 2d); the 1-h change in equivalent surface heating, ΔQ_0; and the entrainment forcing, $-B_E^{ER}d_E^{ER}/F(\delta\rho)$, from (17). All regimes continue if the buoyancy forcing is near neutral ($|L| > 2000$ m). When it is more stable with solar radiation, regime SBL covers steady midday forcing ($|\Delta Q_0| < 0.4Q_0$), regime DBL has a more rapid morning increase, while regime E_W begins with a more rapid afternoon decrease and continues to cover weakly forced ($<5\,\mathrm{cm^3\,s^{-3}}$), shallow ($d_i^* < 0.8d_i$) entrainment into weak stratification (less than 5% of the inversion). When the forcing is more convective, almost all entrainment into strong stratification near the inversion is designated as regime E_C, including for the present the WRW and MRW periods. The exceptions are times of unstable detrainment (Fig. 1), when there is a distinct $B_{MAX} > 0$ at $d_{MAX} > 0$. Although the circumstances may not be unique, these brief DBL periods are identified by a particular combination; namely, solar radiation, Stokes forcing ($\mathrm{La}^{-2} > 0$), very weak entrainment forcing (less than 1 $\mathrm{cm^3\,s^{-3}}$), and cooling that is neither too great ($-Q_0 < 70\,\mathrm{W\,m^{-2}}$), nor increasing too much ($\Delta Q_0 > 0.1\,Q_0$). Thus, regime E_C includes all of JunN ($L < 0$; $\mathrm{La}^{-2} = 0$), as well as AprS and JunS days when entrainment forcing is sufficiently strong.

The regime-dependent construction of flux profiles as polynomial segments, with continuous vertical gradients, is summarized in Table 2. These profiles give $\langle w\theta\rangle^{FP}$ and τ^{FP}, from the surface to beyond the boundary layer, including the detrainment zone. The downwind and crosswind momentum flux components are calculated as

$$\langle wu\rangle_\tau^{FP} = -\tau^{FP}\cos\Omega_\tau^{FP}; \quad \langle wv\rangle_\tau^{FP} = -\tau^{FP}\sin\Omega_\tau^{FP}, \qquad (31)$$

with Ω_τ^{FP} a combination of Ω_τ^{BL} from (20) and Ω_τ^{DZ} from (24), as described in section 5a. Regime SBL's stable boundary layer is

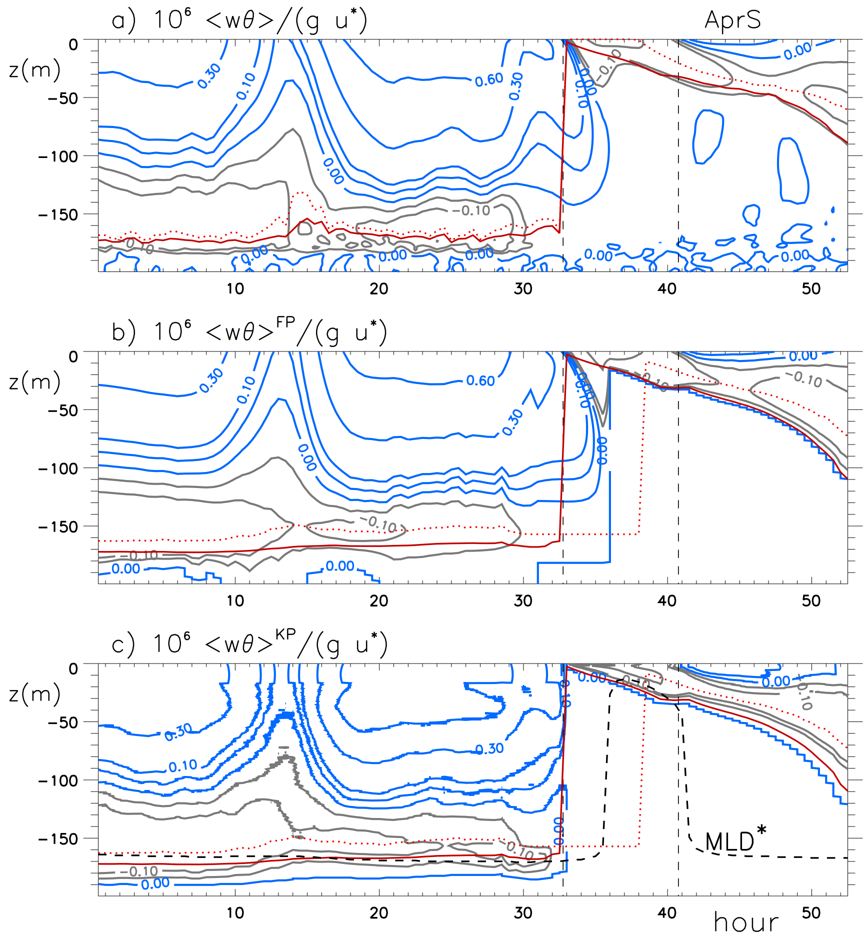

FIG. 13. Comparison of (a) nondimensional buoyancy flux distribution from AprS to the parameterizations of (b) $\langle w\theta\rangle^{\mathrm{FP}}$ (Table 2) and (c) $\langle w\theta\rangle^{\mathrm{KP}}$ from (26). The contours are irregular at 0.0, $\pm$0.05, $\pm$0.10, $\pm$0.30, and 0.60, with negative contours gray. The time series are boundary layer depth h (solid red) and d_E (dotted red) in (a); h^{PAR} (solid) and d_E^{ER} (dotted) constant at its t_{ED} value over regimes DBL and SBL in (b) and (c). Also shown in (c) is a mixed layer depth MLD* based on a small density threshold of 0.006 kg m^{-3} (dashed black). Vertical dashed lines demark the unstable to stable transition at t_{US} = 32.75 h and the return to unstable at t_{SU} = 40.75 h.

the least complicated, because there is no evidence of either entrainment or detrainment, which suggests that boundary layer turbulence and structure are close to equilibrium with the relatively steady forcing. Furthermore, the SBL examples and Fig. 3c show that both $\langle w\theta\rangle$ and τ profiles are nearly linear from the surface to h^{AM}, as indicated in Table 2.

There also appears to be a high degree of equilibrium, including the entrainment, in regime E_C, so it is also relatively straightforward, with nearly linear flux profiles throughout most of the boundary layer. For buoyancy, however, the entrainment point (d_E^{ER}; B_E^{ER}) from section 6a is given by (17), with a consistent $h^{\mathrm{PAR}} = h^{\mathrm{ER}}$. The unique quadratic from (h^{PAR}; B_h^{PAR}) with zero gradient at d_E^{ER} is extended higher to z_M where it meets the linear segment from the surface and the gradient is continuous, as in Table 2. Although Fig. 8 (26 h) shows that the stress magnitude is not yet well represented in the WRW period, $\Omega_\tau^{\mathrm{BL}}$ tracks Ω_τ throughout the boundary layer, despite the 180° deviations from Ω. This example is also representative of JunS's MRW period.

Stress magnitude displays only slight curvature in the Fig. 8 examples, so τ^{FP} is also linear to $h^{\mathrm{PAR}} = h^{\mathrm{ER}}$ in regime E_W (Table 2). However, entrainment into weak diurnal stratification, first through the afternoon then into the night is an F-profile challenge too. The overly strong K-profile entrainment suggests that the fluxes and gradients are not in sufficient equilibrium with the weak entrainment forcing (<5 cm^3 s^{-3}) for K-profile constructs. In particular, the examples from Fig. 8 suggest that afternoon entrainment has a contribution from prior regime SBL generated turbulence, which following section 5a, is related to the buoyancy flux at the time t_{SE} of transition from regime SBL to E_W. As in regime E_C, the contribution from current forcing is characterized by B_E^{ER} at d_E^{ER}. Assuming d_E^{ER} is a viable estimate, the

TABLE 2. Summary of the section 6b construction of F-profile fluxes as polynomial segments and angles from the wind, for each diurnal cycle regimes. A single "+" superscript denotes where a segment's vertical gradient is zero (e.g., $d_E^{\mathrm{ER}+}$), while a double indicates that the curvature is also zero (e.g., d_{MAX}^{++}). Calculated depths are $-z_M$, where the linear and quadratic regime E_C segments match with a continuous gradient, and $-z_B$, where the fluxes and their gradients become zero below h. Table 1 provides references for the key depths, including the regime DBL time integral $\mathrm{d}_{\mathrm{MAX}}(t)$ and the extent of the detrainment zone z_D at a prior entrainment depth.

Regime		$\langle w\theta\rangle^{\mathrm{FP}}$	τ^{FP}	$\Omega_\tau^{\mathrm{FP}}$
E_C	$h = h^{\mathrm{ER}}$	Linear $(0 \to -z_M)$ Quadratic $(-z_M \to d_E^{\mathrm{ER}+} \to h)$ Quadratic $(h \to -z_B^+)$	Linear $(0 \to h)$ Quadratic $(h \to -z_B^+)$	$\Omega_\tau^{\mathrm{BL}}$
E_W	$h = h^{\mathrm{ER}}$	Quadratic $(0 \to d_E^{\mathrm{ER}+})$ Quadratic $(d_E^{\mathrm{ER}+} \to h)$ Quadratic $(h \to -z_B^+)$	Linear $(0 \to h)$ Quadratic $(h \to -z_B^+)$	$\Omega_\tau^{\mathrm{BL}}$
SBL	$h = h^{\mathrm{AM}}$	Linear $(0 \to h)$ Quadratic $(h \to -z_B^+)$	Linear $(0 \to h)$ Quadratic $(h \to -z_B^+)$	$\Omega_\tau^{\mathrm{BL}}(0 \to h)$ $\Omega_\tau^{\mathrm{DZ}}$ (below d^{MKE})
DBL	$-z_D = d_E^{\mathrm{ER}}(t_{\mathrm{ED}})$	Cubic $(0 \to d_{\mathrm{MAX}}^+)$ Cubic $(d_{\mathrm{MAX}}^+ \to -z_D^+)$ Cubic $(-z_D^+ \to d_i^+)$	Cubic $(0 \to d_i^{++})$	$\Omega_\tau^{\mathrm{BL}}(0 \to 2\,\mathrm{m})$ $\Omega_\tau^{\mathrm{DZ}}$ (below 2 m)

entrainment flux throughout regime E_W is, therefore, parameterized by

$$B_E^{\mathrm{PM}} = 0.70\,B_E^{\mathrm{ER}} + B_0(t_{\mathrm{SE}})\left[1 - \frac{d_E^{\mathrm{ER}}}{h^{\mathrm{AM}}(t_{\mathrm{SE}})}\right], \qquad (32)$$

where the second term is not allowed to be positive, because it represents the buoyancy flux at time t_{SE} and depth d_E^{ER}, assuming a linear regime SBL profile to h^{AM}. This relation is evaluated in Fig. 11b over all of regime E_W for both AprS (red) and AprN (blue). The 0.70 coefficient is chosen to give good estimates of the strongest entrainment from early in the regime, and to keep the AprS agreement within a factor of 2. A quadratic from the surface to zero gradient at the entrainment point $(d_E^{\mathrm{ER}}; B_E^{\mathrm{PM}})$ gives $\langle w\theta\rangle^{\mathrm{FP}}$ in the top segment of regime E_W, and a smooth connection to another quadratic from d_E^{ER} to h^{ER}, as indicated in Table 2.

In regimes E_C, E_W, and SBL, there is a meaningful boundary layer depth, h^{PAR}, where (29) can be used to give estimates of nonzero fluxes, B_h^{PAR} and τ_h^{PAR}. Deeper, there is a unique quadratic that matches these fluxes and their gradients, as given from the segment above, at h^{PAR} and goes to zero with zero gradient at a computed depth $-z_B$. However, in the F profiles (dashed blue) of Figs. 8 and 10, $\tau_h^{\mathrm{PAR}} = 0$, but as a demonstration of how the buoyancy flux could go to zero at depth, $B_h^{\mathrm{PAR}} = \langle w\theta\rangle$ at $z = -h^{\mathrm{PAR}}$.

The shortcomings of K-profile fluxes indicate that regime DBL is far from equilibrium, such that fluxes are nonlocal in time as well as depth. Hence, they do not reflect a boundary layer depth. Nonetheless, complete F profiles are constructed, as shown in Table 2. First, (22) is integrated from t_{ED} to give a deepening d_{MAX} (Fig. 9d), then the detrainment rule (23), as verified in Fig. 11, gives B_{MAX} diminishing with time. Also, an earlier entrainment depth and buoyancy flux at time t_{ED} remain a constant endpoint throughout DBL. Curvature in flux profiles may also reflect dependencies on time history. In particular, regime DBL profiles of $\langle w\theta\rangle^{\mathrm{FP}}$ are cubic functions of depth over three segments that connect with continuous gradients at both d_{MAX} and $d_E(t_{\mathrm{ED}})$. The deepest segment is cosmetic rather than physical, but smoothly goes to zero at the inversion. Also, τ^{FP} is a cubic from u^{*2} at the surface to zero at the inversion, where both the gradient and curvature are also zero.

c. Evaluation

For evaluation purposes, $\upsilon_s = 0.1\,\mathrm{cm}^2\,\mathrm{s}^{-1}$ in (29), in rough accord with regime E_C. Although primarily for cosmetic purposes, this diffusivity is consistent with purposeful tracer releases in the pycnocline (Ledwell et al. 1993), but is only about one-fifth the regime E_W values. In general τ_h^{PAR} is negligible because of the small shear in (29), so direction issues are avoided with $\upsilon_m = 0$. At d_E^{ER}, $H(d)$ in (26) is zero, so in regime E_C $\langle w\theta\rangle^{\mathrm{FP}}$ and $\langle w\theta\rangle^{\mathrm{KP}}$ are equal by construction, even though the latter may not be the local negative extremum (e.g., Fig. 8).

Figure 13 shows that a number of features seen in the diurnal cycle of buoyancy flux in the boundary layer are represented by both schemes. Examples include the collapse of the boundary layer at t_{US}, variations in the vertical extent of the entrainment zone (negative gray contours), as well as the depth and strength of entrainment. One of the more obvious successes is the response to the daytime solar heating between hours 9 and 17, while the buoyancy forcing remains unstable. At all depths in Fig. 13c the primary response is that of Γ_s from (8) to variations in B_0 as the sun rises then sets. This response only affects Fig. 13b directly at d_E^{ER}, which also rises, but not by as much as d_E (Fig. 13a). The discontinuity at the surface layer limit of (25) is readily apparent throughout Fig. 13c.

The statistics compiled in Table 3 provide more quantitative evaluations of different regimes and layers, with row numbers provided for reference. They show the F-profile fluxes to have higher fidelity; sometimes significantly. For example (row A.1), in the surface layer of all regimes the $\langle w\theta\rangle^{\mathrm{FP}}$ regression gives a correlation coefficient greater than 0.99, a slope very near unity and intercept near zero, there is no mean bias, $R_M = 1.00$, and a small root-mean-square difference, $\delta_{\mathrm{rms}} = 0.024$. Even though surface layer fluxes are strongly constrained by the surface boundary conditions, the corresponding results from $\langle w\theta\rangle^{\mathrm{KP}}$

TABLE 3. Quantitative evaluation of fluxes over various layers in the referenced figures; F profile (FP, middle) and K profile (KP, bottom) against LES (top). The root-mean-square difference is δ_{rms}, the ratio of the means R_M is the mean bias, and the depth–time correlation coefficient is $r_{z,t}$. These results are referenced by row number, which are grouped according to the flux; buoyancy (A.1–A.8), downwind momentum (B.1–B.8), and crosswind (C.1–C.8).

Vertical Flux	Layer	Regimes	Instances	PAR	δ_{rms}	R_M	$r_{z,t}$	Row
$\langle w\theta\rangle(10^6/g\,u^*)$ (Fig. 13)	Surface ($\sigma < \varepsilon$)	E_C	1323	FP	0.024	1.00	0.994	A.1
				KP	0.066	1.12	0.988	A.2
	Deep boundary ($\varepsilon < \sigma < 1$)	E_C	8457	FP	0.047	0.92	0.98	A.3
				KP	0.088	1.24	0.96	A.4
	Boundary ($\sigma < 1$)	SBL + E_W	1788	FP	0.048	1.16	0.96	A.5
				KP	0.074	1.17	0.91	A.6
	Detrainment [above $d_E(t_{\mathrm{ED}})$]	DBL	1429	FP	0.086	0.93	0.95	A.7
				KP	0.106	1.31	0.77	A.8
$-\langle wu\rangle_\tau/u^{*2}$ (Fig. 14)	Surface ($\sigma < \varepsilon$)	E_C	1323	FP	0.14	1.07	0.91	B.1
				KP	0.66	0.38	0.17	B.2
	Deep boundary ($\varepsilon < \sigma < 1$)	E_C	8457	FP	0.19	1.38	0.90	B.3
				KP	0.39	0.66	0.47	B.4
	Boundary ($\sigma < 1$)	SBL + E_W	1788	FP	0.06	1.09	0.99	B.5
				KP	0.33	1.45	0.75	B.6
	Detrainment [above $d_E(t_{\mathrm{ED}})$]	DBL	1429	FP	0.15	1.18	0.86	B.7
				KP	0.32	0.70	0.38	B.8
$-\langle wv\rangle_\tau/u^{*2}$ (Fig. 15)	Surface ($\sigma < \varepsilon$)	E_C	1323	FP	0.20	0.50	0.91	C.1
				KP	0.75	1.57	−0.59	C.2
	Deep boundary ($\varepsilon < \sigma < 1$)	E_C	8457	FP	0.25	0.60	0.64	C.3
				KP	0.55	0.55	−0.22	C.4
	Boundary ($\sigma < 1$)	SBL + E_W	1788	FP	0.12	1.57	0.61	C.5
				KP	0.27	0.64	0.55	C.6
	Detrainment [above $d_E(t_{\mathrm{ED}})$]	DBL	1429	FP	0.12	1.76	0.84	C.7
				KP	0.20	−0.45	0.36	C.8

(row A.2) show a high bias ($R_M = 1.12$) and nearly a factor of 3 greater δ_{rms}; a quantitative reflection of the effects of variable forcing on the flux–profile relationships (25).

There is less fidelity in the more weakly constrained deeper boundary layer. For example, during regime E_C, the positive bias above about 70 m in Fig. 13c, leads to $R_M = 1.24$ (row A.4), while there is a low mean bias in Fig. 13b ($R_M = 0.92$) and about half the δ_{rms} (row A.3), but the respective correlations fall only slightly to 0.96 and 0.98. Prominent issues in Fig. 13c are the overly negative fluxes in regime SBL and excessive entrainment in regime E_W, which are quantified by $R_M = 1.17$, as well as by nearly twice the δ_{rms} and the reduced correlation (row A.6), than found for $\langle w\theta\rangle^{\mathrm{FP}}$ (row A.5), whose regime E_W behavior is directly governed by B_E^{PM} computed from (32) and evaluated in Fig. 11.

The full depth of regime DBL is represented only by $\langle w\theta\rangle^{\mathrm{FP}}$. Most importantly, these values are maintained at comparable levels to Fig. 13a for some time after the boundary layer collapse at t_{SU}, including at the depth of the maximum (Fig. 9d), despite the negative buoyancy flux nearer the surface (e.g., Fig. 10, hour 34). In particular, they display a similar decay to zero at all depths below the boundary layer by hour 36, as governed by $B_{\mathrm{MAX}}^{\mathrm{PAR}}$ (23). However, the behavior prior to the collapse is not captured as well by either scheme, though a subsurface maximum does develop near 20 m in Fig. 13b, but the decrease below is too gradual (e.g., Fig. 10, hour 32). The effect of $\langle w\theta\rangle^{\mathrm{KP}} = 0$ in the detrainment zone below the boundary layer is quantified by the statistics in Table 3 (row A.8). The correlation is only 0.77, compared to 0.95 for F-profile (row A.7), and δ_{rms} is about 25% more.

d. Momentum flux components

Both the magnitude and orientation of the stress vector contribute to errors in parameterized momentum flux components. Clear manifestations of each being dominant are evident in regimes SBL and E_W. In particular, Fig. 14c values greater than 1 after hour 42 are due to very large shears in the calculations of τ^{KP} from (27) and (28). On the other hand, the tendency for $\Omega_\tau^{\mathrm{KP}}$ to track $(-\Omega_W)$ leads to the strange behavior of Fig. 15c below the surface layer, where there is a zero contour near 15 m with a $-\langle wv\rangle_\tau^{\mathrm{KP}}$ maximum at about $\sigma = 0.5$. Thus, both K-profile components are poor representations of these regimes, with low correlations (0.75 and 0.55) and sizable δ_{rms} (0.33 and 0.27) in Table 3 (rows B.6 and C.6). In contrast, Figs. 14a and 14b are more highly correlated (0.99), with a much lower $\delta_{\mathrm{rms}} = 0.06$, and little mean bias (row B.5). The small differences between $\Omega_\tau^{\mathrm{FP}}$ and Ω_τ, do have more effect on the sine function of (31) than the cosine, so Figs. 15a and 15b are less correlated (0.61), with higher $\delta_{\mathrm{rms}} = 0.12$ and more mean bias (row C.5).

Figures 14a and 14b both show the downwind momentum flux decreasing monotonically from u^{*2}, and changing sign at about 10 m in the WRW period, but Fig. 14c differs markedly, especially in the surface layer where variations in the angle Ω_τ, are tracked much better by $\Omega_\tau^{\mathrm{FP}}$ than by $\Omega_\tau^{\mathrm{KP}}$. As a consequence, the statistics of Table 3 from the surface layer of

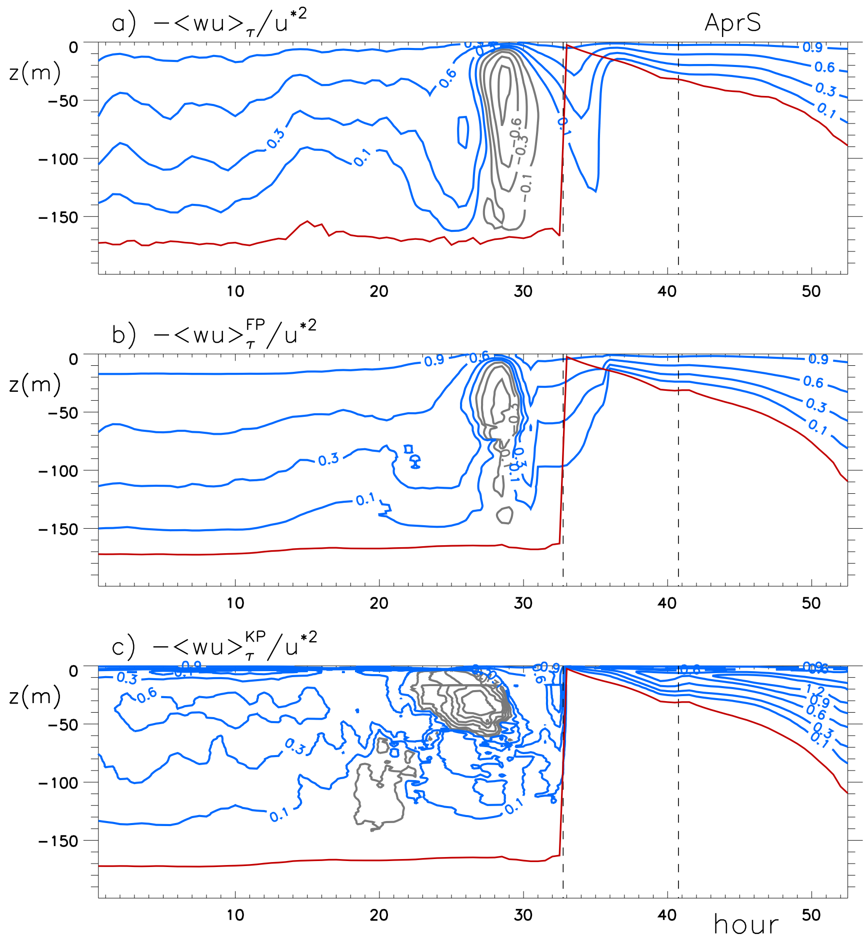

FIG. 14. Comparison of (a) downwind momentum flux $-\langle wu\rangle_\tau$ to parameterized distributions of (b) $-\langle wu\rangle_\tau^{FP} = \tau^{FP}\cos\Omega_\tau^{FP}$ (Table 2) and (c) $-\langle wu\rangle_\tau^{KP}$ from rotating (27) and (28). The contours are nonzero at ±0.10, ±0.30, ±0.6, ±0.90, ±1.20, and ±1.50, with negative contours gray. The time series are boundary layer depth h (solid red) in (a) and h^{PAR} in (b) and (c).

regime E_C, for example, show that both F-profile components (rows B.1 and C.1) are quite representative. In particular, the correlation coefficients are high (0.91) and δ_{rms} is no more than 0.20, though there is a low mean crosswind bias. The failure of Ω_τ^{KP} and downgradient viscosity near the surface is demonstrated by the loss of correlation (rows B.2 and C.2), and the factor of about 4 greater δ_{rms}, despite the strong constraint on τ^{KP} from (25).

Below the surface layer of regime E_C the $-\langle wu\rangle_\tau^{KP}$ statistics (row B.4) are markedly improved, but still inferior to the F-profiles (row B.3), as are those of $-\langle wv\rangle_\tau^{KP}$ (row C.4 compared to C.3), especially the negative correlation. Even though these statistics include the WRW period, they quantify the impression from 14, that both schemes are reasonable representations of the downwind momentum flux at these depths. A remarkable feature of the WRW period of Fig. 14a is the positive downwind momentum flux (gray contours) across the entire boundary layer, which is well reproduced by $-\langle wu\rangle_\tau^{FP} < 0$ in Fig. 14b, as to a lesser degree is the corresponding pattern of crosswind, $-\langle wv\rangle_\tau^{FP} > 0$ in Fig. 15b. Coriolis effects, weak winds, and counterinertial rotation contribute to this behavior, but the essential information appears to be contained in Ω_τ^{BL} (e.g., Fig. 8, hour 26).

Momentum fluxes in the detrainment zone above $d_E(t_{ED})$ are short lived, and so perhaps negligible for many purposes. Should they become important, however, the qualitative agreement evident between Figs. 14a and 14b and between Figs. 15a and 15b, offers a path forward, with the angle Ω_τ^{DZ} the key ingredient. A comparison between rows B.7 and B.8 and between rows C.7 and C.8 of Table 3 provides a quantitative measure of present success.

e. Comparative case evaluation

Evaluations of boundary layer ($\sigma < 1$) fluxes, including stress magnitude, τ, from different cases are quantified in Table 4 by the bracketed δ_{rms}, and by the correlations in square brackets. For AprS, the higher fidelity of F-profile scheme in Table 3 is reflected in the smaller δ_{rms} and higher correlations,

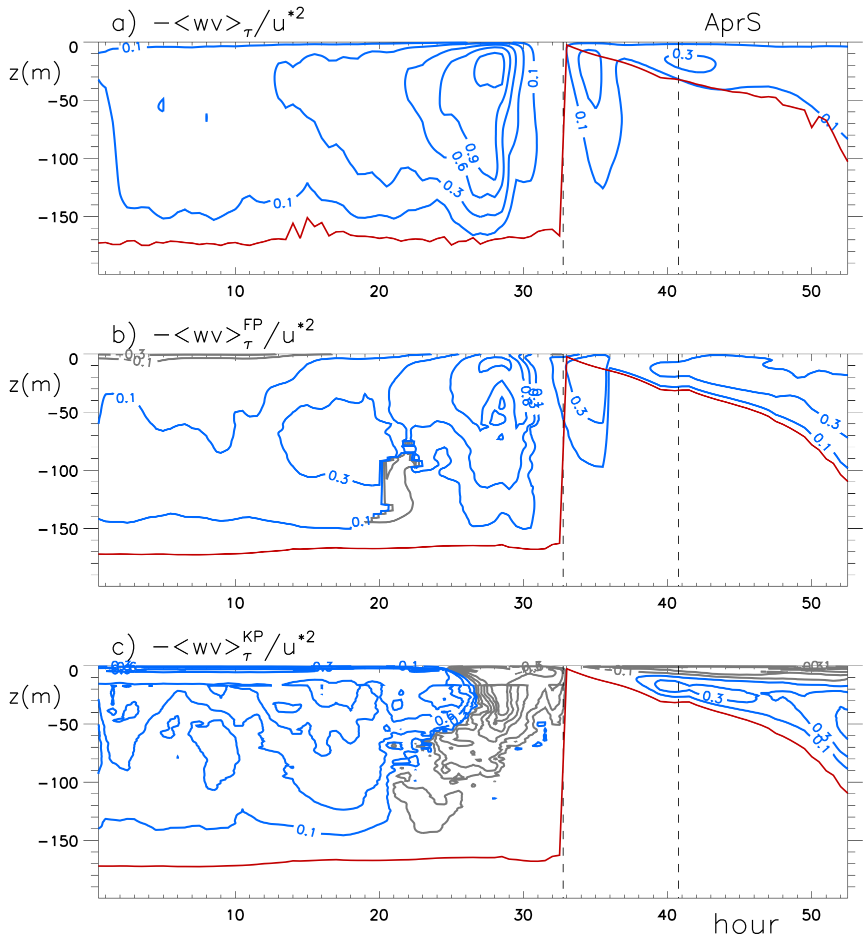

FIG. 15. As in Fig. 14, but for the crosswind momentum flux $\langle wv\rangle_\tau$ and the parameterized $\langle wv\rangle_\tau^{\mathrm{FP}} = -\tau^{\mathrm{FP}}\sin\Omega^{\mathrm{FP}}$ and $\langle wv\rangle_\tau^{\mathrm{KP}}$.

compared to the K-profile, for all four fluxes. This relative performance is closely mirrored in the buoyancy flux from the four other cases, but in the momentum flux only from the other two Stokes forced cases, except for the comparatively high D24S $\langle wv\rangle_\tau^{\mathrm{KP}}$ correlation (0.70), despite a high $\delta_{\mathrm{rms}} = 0.48$. This anomaly is a consequence of K-profile values that are as much as a factor of 4 too high from late in D24S. Thus, it appears as if the shear is not responding to the falling wind as fast as the stress, such that τ^{KP} significantly exceeds τ over much of the boundary layer and the substantial $\delta_{\mathrm{rms}} = 0.84$ in Table 4 is accompanied by a loss of correlation.

The Table 4 F-profile statistics from AprS compared to AprN and from JunS compared to JunN, quantify the improved performance of all four fluxes with Stokes forcing, over cases without. In the idealized, but unphysical absence of Stokes forcing during AprN and JunN, there is much closer alignment of the wind, stress, and shear vectors throughout the boundary layer. Therefore, (8) provides better estimates of $\langle wv\rangle^{\mathrm{KP}} = \Gamma_v$ than it does in the Stokes cases, especially near the surface. This improved fidelity is quantified by the decreases in K-profile δ_{rms} relative to the corresponding Stokes cases, in contrast to the increases in the F-profile values. Considering τ for example, a decrease from 0.53 in AprS to 0.38 in AprN is associated with an F-profile increase from 0.19 to 0.38. In general the AprN and JunN momentum fluxes from both schemes are comparable, though the K-profile δ_{rms} becomes the smaller for all three quantities in JunN.

7. Discussion and conclusions

The boundary layer depth is an important upper-ocean parameter, because it bounds the extent of large surface forced local and nonlocal turbulent transports through the shape function G_C, and it directly scales the mixing coefficients $K_{m,s}$ (7). However, the multiple options in Table 1 can be problematic. Neither the inversion depth, nor a mixed layer depth is a viable proxy, because they do not track the collapse with stable buoyancy forcing, for example. The depth h^{L19} is not appropriate throughout much of regimes DBL and SBL when it lies beyond the d_{MKE} bound (Fig. 9b), and of regime E_W when Fig. 7b shows it is too deep to be consistent with the entrainment rule (17). Similarly, h^{KPP} is overly deep in regime E_W (Fig. 7c). In contrast, both the entrainment depth and buoyancy flux are robust diagnostics of LES buoyancy flux

TABLE 4. Evaluation of F-profile (FP) and K-profile (KP) fluxes throughout the boundary layer ($\sigma = -z/h < 1$) of different cases, as quantified by the root-mean-square difference from the LES, $\delta_{\rm rms}$ (parentheses), and the depth–time correlation coefficient (square brackets). All regimes are included, except the June MRW period.

		AprS	JunS	D24S	AprN	JunN
	Instances	12 252	12 332	9245	11 586	12 395
		($\delta_{\rm rms}$) [$r_{z,t}$]	($\delta_{\rm rms}$) [$r_{z,t}$]	($\delta_{\rm rms}$) [$r_{z,t}$]	($\delta_{\rm rms}$) [$r_{z,t}$]	($\delta_{\rm rms}$) [$r_{z,t}$]
$\langle w\theta\rangle(10^6/g\,u^*)$	FP	(0.05) [0.98]	(0.05) [0.95]	(0.06) [0.96]	(0.09) [0.95]	(0.06) [0.93]
	KP	(0.09) [0.97]	(0.14) [0.87]	(0.07) [0.95]	(0.11) [0.91]	(0.09) [0.90]
$-\langle wu\rangle_\tau/u^{*2}$	FP	(0.17) [0.93]	(0.18) [0.93]	(0.14) [0.96]	(0.33) [0.62]	(0.18) [0.86]
	KP	(0.41) [0.47]	(0.51) [0.69]	(0.75) [0.57]	(0.30) [0.66]	(0.16) [0.88]
$-\langle wv\rangle_\tau/u^{*2}$	FP	(0.22) [0.64]	(0.16) [0.83]	(0.18) [0.41]	(0.34) [0.44]	(0.24) [0.72]
	KP	(0.53) [−0.2]	(0.40) [0.34]	(0.48) [0.70]	(0.40) [0.30]	(0.14) [0.59]
τ/u^{*2}	FP	(0.19) [0.84]	(0.18) [0.88]	(0.10) [0.95]	(0.38) [0.66]	(0.25) [0.85]
	KP	(0.53) [0.74]	(0.58) [0.71]	(0.84) [−0.2]	(0.38) [0.60]	(0.14) [0.90]

profiles, with $h = h^{\rm BL}$, consistent with (26). However, the parameterizations of these depths are not straightforward, especially when the degree of equilibrium is a factor. The entrainment rule does give a parameterized $h^{\rm ER}$ and consistent $d_E^{\rm ER}$, when the buoyancy forcing is unstable. The wide range of forcing conditions, with and without Stokes drift, involved in the development of this rule lends some credence to these depths. In stable conditions the time history of the forcing gives a defensible $h = h^{\rm AM}$ from (21), as well as $d_{\rm MAX}$ (22) in regime DBL, but these empirical relationships from AprS and AprN may not be universal. Nonetheless, $h^{\rm PAR} = h^{\rm AM}$ is appropriate in the regime SBL example of Fig. 10, though $\kappa L^*(t_{\rm DS})$ may prove to be a more robust alternative (Fig. 9b).

In general, the momentum flux is aligned with neither the wind, nor the shear, though at depth the stress vector tends to remain more oriented with the wind than to the veering shear, such there can be a significant across-shear component. A major effect of Stokes forcing is to accentuate the misalignment between the stress and shear vectors, especially near the surface where the Stokes drift and shear are greatest. For example, during regimes SBL and E_W of AprS, the angle between the wind and shear Ω_W is greater than 45° near 4-m depth. The Hughes et al. (2020) observations of shear in the diurnal warm layer also show $\Omega_W > 45°$ below 3 m. Thus, the absence of across-shear momentum flux is a possible explanation of why not one of four turbulence parameterizations correlates with their observations. Hence, downgradient eddy viscosity does not appear to be a reliable assumption. Therefore, a fortunate finding is that throughout the boundary layer the angle Ω_τ of the stress from the wind is highly correlated with the angle $\Omega_\tau^{\rm BL}$ from (20); a linear combination of the orientations relative to the wind of the Lagrangian shear to the surface and the local (5 m) Eulerian shear. However, below the boundary layer of regime SBL and throughout the detainment zone, Ω_τ is better tracked by another empirical angle $\Omega_\tau^{\rm DZ}$ from (24). Such empirical angles allow the novel formulation of the momentum flux as a magnitude and a direction that deviates from the orientation of the shear. This direction could be used with any momentum flux parameterization of either the magnitude, or a single component. For example, should it be combined with $\langle wu\rangle^{\rm KP}$ from (27), or with a K-profile stress magnitude, there would be no need to parameterize Γ_v, and hence to improve (8) near the surface.

The development environment for the entrainment and detrainment rules is limited to the Southern Ocean in autumn, but there is a wide range of variable forcing. Thus, the detrainment rules (22) and (23) evaluated in Fig. 11a, include unstable periods of AprS and JunS, as well as the more familiar AprS detrainment below a stable boundary layer. The full range, from extreme wave conditions, including significant swell (L19), to idealized calm seas is involved in the development of the entrainment rule (17). Although the Coriolis parameter is fixed, a variety of rotational interactions, such as cos $\Omega^{\rm PAR}$ in (30), is provided by the counterinertial wind rotation of the WRW period, by the subsequent inertial rotation and by the falling wind of D24S. This rule also applies to the very different entrainment of regimes E_C and E_W, but it should not be regarded as universal, pending further development. In particular, the function $F(\delta\rho)$ in (17) remains to be determined, but the 0.7 coefficient of (32) is consistent with the function decreasing to zero as the stratification at the entrainment depth vanishes. As a preliminary examination of shallower, much stronger stratification and dominant wind forcing, the entrainment rule has been applied to the Watkins and Whitt (2020) simulations of a hurricane over a coastal shelf. Compared to early in AprS and AprN, the stratification at the inversion is stronger by about a factor of 10, the entrainment forcing of (17) is about the same, even though the integrated TKE production to the inversion is about an order of magnitude higher. The entrainment B_E is order 100 times greater, and the boundary layer depth is only about one-tenth. Thus, these results would fit well within the spread of Fig. 6, with $F(\delta\rho)$ equal to about 10, at 10 times greater stratification. In the parlance of the dimensional analysis of similarity theory, this finding supports regarding surface layer TKE source integrals as independent variables (L19a), that determine the dependent variables associated with entrainment, at least in regime E_C. Alternatively, integrals to the inversion (Fig. 1) would yield consistent results with no change in $F(\delta\rho)$. However, these deeper integrals have yet to be parameterized.

From section 4, the fractions of positive boundary layer TKE production by Eulerian shear, Stokes shear and buoyancy that go to increasing potential energy rather than dissipating, are 0.020, 0.035, and 0.27, respectively. An interpretation is that buoyancy produces TKE at the largest scales and hence is most efficient at increasing potential energy by entrainment. Furthermore, Langmuir turbulence has larger scales and is more efficient than turbulent motions driven by Eulerian shear. Thus, the effects of smaller-scale, near-surface processes, such as wave breaking and solar penetration, may be relatively small, especially for deep boundary layers. In pure convection ($u^* \rightarrow 0$) the ratio B_E/B_0 from (17), ranges from about 0.10 to 0.15, depending on the ratio (h/d_E) in Fig. 7a. Considering this range is an extrapolation from strong wind and wave forcing, with ocean stratification and $F(\delta\rho) = 1$, it is roughly consistent with the empirical 0.2 from atmospheric convection (section 4).

The K-profile fluxes of section 6 are based on Monin–Obukhov similarity theory in the surface layer, including Stokes effects from L19a as updated in section 6, on rules for local and nonlocal (8) boundary layer transport developed in L19b, and on a parameterized boundary layer depth h^{PAR}. They do not yet extend into the detrainment zone below the boundary layer. The parameterizations are empirical and assume that the forcing, fluxes and local shear and stratification are in sufficient equilibrium for eddy diffusivity and viscosity concepts to be applicable. Accordingly, they appear to be most reliable during regimes SBL and E_C apart from the WRW and MRW periods, less so for the afternoon entrainment of regime E_W, and unreliable during regime DBL and late in D24S. The prospect of improving detrainment is not promising, because there is no signature of a distinct boundary layer depth in any turbulence distribution.

An interpretation of the differences between schemes in the Li et al. (2019) comparison is that realistic forcing has different effects when equilibrium assumptions may not be valid. In contrast, the F profiles are constructed to apply to nonequilibrium boundary layers and detrainment zones by incorporating some time history. Specific examples are h^{AM} (21), d_{MAX} (22), B_{MAX} (23), and B_E^{PM} (32), with the regime determination (section 6b) a key aspect. The profiles of Table 2 also rely on parameterized stress directions such as $\Omega_\tau^{\mathrm{BL}}$, to partition the τ profile into momentum flux components. In addition, K-profile fluxes at the entrainment depth where Figs. 8 and 13 show them to be most reliable, are used to determine d_E^{PAR}, B_E^{PAR}, and h^{ER}, consistent with the entrainment rule (17). In principle, these values could be supplied by any boundary layer scheme, including STM. In any case, the empirical coefficients and criteria from limited cases may not always be applicable. Another possibility would be to use d_{MKE}, as a scale for the vertical penetration of the stress during unstable detrainment (Fig. 10; hour 32). The specific functions of Table 2 do serve as examples to demonstrate how curvature can accommodate nonequilibrium, but there could be more widely applicable alternatives, especially for counterinertial wind rotation, such as the April WRW period with $\tau > u^{*2}$ (Fig. 10; hour 32).

The F profiles are constructed with continuous first derivatives, so that accelerations and buoyancy tendencies are given directly at any depth, rather than as flux differences that strongly depend on gradients. The consequences for numerical stability, adaptive vertical grids and conservation could be substantial. Also, it would be straightforward to solve a heat equation very near surface, so that the evolving temperature would be most appropriate for bulk formula calculations of the surface sensible and latent heat fluxes. This temperature could be combined with an estimate of the cool skin effect (Fairall et al. 1996) to give the sea surface temperature governing the emission of longwave radiation.

Both parameterizations of section 6 have been applied with some success to three flavors of diurnal cycle. The most important is the one April day when solar radiation is sufficient for the surface buoyancy forcing to become stable and the boundary layer to collapse with detrainment below. Diurnal effects are negligible over the first April day and the second June day when the forcing remains unstable and strong, but there are discernible signals when the unstable forcing is weak during regime DBL of the first June day. However, additional cases with much stronger noon heating found in summer or at lower latitudes, with penetrating solar radiation, and with stronger wind are needed for widespread verification. Nonetheless, the prospect of a general mixing scheme applicable to all regimes is supported by the smooth and orderly time–depth flux variations of Figs. 13–15, with past history clearly involved (Figs. 3, 8, and 10), but not always eddy diffusivity and viscosity that rely on equilibrium with local stratification and shear.

Acknowledgments. This work was made possible by support from the U.S. Department of Energy (DOE) under solicitation: DE-FOA-0001036, Climate and Earth System Modeling: SciDAC and Climate Variability and Change, Grant SC-00126005. The 1-h averaged data are available half-hourly from Version 1.0. UCAR/NCAR DASH Repository (https://doi.org/10.5065/87n8-9r86). The other principal investigators—Todd Ringler, Gokhan Danabasoglu, and Matt Long—are gratefully acknowledged, as are the contributions of Alice DuVivier and Justin Small. A special thanks to Dan Whitt for providing results from the Watkins and Whitt (2020) hurricane simulations archived at https://doi.org/10.6084/m9.figshare.12486056.v5 (irene-les-mean-2304 × 84all.nc). The National Center for Atmospheric Research (NCAR) is sponsored by the National Science Foundation. The four SOFS simulations were forced, initialized and evaluated with data sourced from Australia's Integrated Marine Observing System (IMOS) - IMOS is enabled by the National Collaborative Research Infrastructure Strategy (NCRIS). They utilized resources of the National Energy Research Scientific Computing Center, a DOE Office of Science User Facility supported by the Office of Science of the U.S. Department of Energy under Contract DE-AC02-05CH11231. The idealized simulations utilized high-performance computing on Yellowstone (ark:/85065/d7wd3xhc) provided by NCAR's Computational and Information Systems Laboratory.

REFERENCES

Ball, F., 1960: Control of the inversion height by surface heating. *Quart. J. Roy. Meteor. Soc.*, **86**, 483–494, https://doi.org/10.1002/qj.49708637005.

Burchard, H., and Coauthors, 2008: Observational and numerical modeling methods for quantifying coastal ocean turbulence and mixing. *Prog. Oceanogr.*, **76**, 399–442, https://doi.org/10.1016/j.pocean.2007.09.005.

Canuto, V., Y. Cheng, and A. Howard, 2009: Non-local ocean mixing model and a new plume model for deep convection. *Ocean Modell.*, **16**, 28–46, https://doi.org/10.1016/j.ocemod.2006.07.003.

Cheng, Y., V. Canuto, and A. Howard, 2002: An improved model for the turbulent PBL. *J. Atmos. Sci.*, **59**, 1550–1565, https://doi.org/10.1175/1520-0469(2002)059<1550:AIMFTT>2.0.CO;2.

Craik, A., and S. Leibovich, 1976: A rational model for Langmuir circulations. *J. Fluid Mech.*, **73**, 401–426, https://doi.org/10.1017/S0022112076001420.

Danabasoglu, G., W. Large, J. Tribbia, P. Gent, B. Briegleb, and J. McWilliams, 2006: Diurnal coupling in the tropical oceans of CCSM3. *J. Climate*, **19**, 2347–2365, https://doi.org/10.1175/JCLI3739.1.

de Boyer Montégut, C., 2004: Mixed layer depth over the global ocean: An examination of profile data and a profile-based climatology. *J. Geophys. Res. Oceans*, **109**, C12003, https://doi.org/10.1029/2004JC002378.

Deardorff, J., 1972: Theoretical expression for the countergradient vertical heat flux. *J. Geophys. Res.*, **77**, 5900–5904, https://doi.org/10.1029/JC077i030p05900.

Fairall, C., E. Bradley, J. Godfrey, G. Wick, and J. Edson, 1996: Cool-skin and warm-layer effects on sea surface temperature. *J. Geophys. Res.*, **101**, 1295–1308, https://doi.org/10.1029/95JC03190.

Filipiak, M., C. Merchant, H. Kettle, and P. L. Borgne, 2012: An empirical model for the statistics of sea surface diurnal warming. *Ocean Sci.*, **8**, 197–209, https://doi.org/10.5194/os-8-197-2012.

Grant, A., and S. Belcher, 2009: Characteristics of Langmuir turbulence in the ocean mixed layer. *J. Phys. Oceanogr.*, **39**, 1871–1887, https://doi.org/10.1175/2009JPO4119.1.

Harcourt, R., 2015: An improved second-moment closure model of Langmuir turbulence. *J. Phys. Oceanogr.*, **45**, 84–103, https://doi.org/10.1175/JPO-D-14-0046.1.

——, and E. D'Asaro, 2008: Large-eddy simulation of Langmuir turbulence in pure wind seas. *J. Phys. Oceanogr.*, **38**, 1542–1562, https://doi.org/10.1175/2007JPO3842.1.

Högström, U., 1988: Non-dimensional wind and temperature profiles in the atmospheric surface layer. *Bound.-Layer Meteor.*, **42**, 55–78, https://doi.org/10.1007/BF00119875.

Hughes, K., J. Moum, and E. Shroyer, 2020: Evolution of the velocity structure in the diurnal warm layer. *J. Phys. Oceanogr.*, **50**, 615–631, https://doi.org/10.1175/JPO-D-19-0207.1.

Kantha, L., and C. Clayson, 1994: An improved mixed layer model for geophysical applications. *J. Geophys. Res.*, **99**, 25 235–25 266, https://doi.org/10.1029/94JC02257.

Kraus, E., and J. Turner, 1967: A one-dimensional model of the seasonal thermocline, II. The general theory and its consequences. *Tellus*, **19**, 98–106, https://doi.org/10.3402/tellusa.v19i1.9753.

Kukulka, T., A. Plueddeman, and P. Sullivan, 2013: Inhibited upper ocean restratification in nonequilibrium swell conditions. *Geophys. Res. Lett.*, **40**, 3672–3676, https://doi.org/10.1002/grl.50708.

Large, W., 1996: An observational and numerical investigation of the climatological heat and salt balances at OWS Papa. *J. Climate*, **9**, 1856–1876, https://doi.org/10.1175/1520-0442(1996)009<1856:AOANIO>2.0.CO;2.

——, and J. Caron, 2015: Diurnal cycling of sea surface temperature, salinity, and current in the CESM coupled climate model. *J. Geophys. Res. Oceans*, **120**, 3711–3729, https://doi.org/10.1002/2014JC010691.

——, J. McWilliams, and S. Doney, 1994: Oceanic vertical mixing: A review and a model with a nonlocal boundary layer parameterization. *J. Atmos. Sci.*, **32**, 363–403, https://doi.org/10.1029/94RG01872.

——, E. Patton, A. DuVivier, and P. Sullivan, 2019a: Similarity theory in the surface layer of large-eddy simulations of the Southern Ocean with waves. *J. Phys. Oceanogr.*, **49**, 2165–2187, https://doi.org/10.1175/JPO-D-18-0066.1.

——, ——, and P. Sullivan, 2019b: Nonlocal transport and implied viscosity and diffusivity throughout the boundary layer in LES of the Southern Ocean with surface waves. *J. Phys. Oceanogr.*, **49**, 2631–2652, https://doi.org/10.1175/JPO-D-18-0202.1.

——, ——, A. DuVivier, and P. Sullivan, 2021: Large eddy simulation of the southern ocean. Version 1.0. UCAR/NCAR DASH Repository, accessed 22 April 2021, https://doi.org/10.5065/87n8-9r86.

Ledwell, J., A. Wilson, and C. Low, 1993: Evidence for slow mixing across the pycnocline from an open-ocean tracer-release experiment. *Nature*, **364**, 701–703, https://doi.org/10.1038/364701a0.

Li, Q., and B. Fox-Kemper, 2017: Assessing the effects of Langmuir turbulence on the entrainment buoyancy flux in the ocean surface boundary layer. *J. Phys. Oceanogr.*, **47**, 2863–2886, https://doi.org/10.1175/JPO-D-17-0085.1.

——, and Coauthors, 2019: Comparing ocean boundary vertical mixing schemes including Langmuir turbulence. *J. Adv. Model. Earth Syst.*, **11**, 3545–3592, https://doi.org/10.1029/2019MS001810.

Martin, P., 1985: Simulation of the mixed layer at OWS November and Papa with several models. *J. Geophys. Res.*, **90**, 903–916, https://doi.org/10.1029/JC090iC01p00903.

McWilliams, J., P. Sullivan, and C.-H. Moeng, 1997: Langmuir turbulence in the ocean. *J. Fluid Mech.*, **334**, 1–30, https://doi.org/10.1017/S0022112096004375.

Mellor, G., and T. Yamada, 1982: Development of a turbulence closure model for geophysical fluid problems. *Rev. Geophys.*, **20**, 851–875, https://doi.org/10.1029/RG020i004p00851.

Moeng, C.-H., 1984: A large-eddy simulation model for the study of planetary boundary-layer turbulence. *J. Atmos. Sci.*, **41**, 2052–2062, https://doi.org/10.1175/1520-0469(1984)041<2052:ALESMF>2.0.CO;2.

Monin, A., and A. Obukhov, 1954: Basic laws of turbulent mixing in the surface layer of the atmosphere. *Tr. Akad. Nauk SSSR Geophiz.*, **24**, 163–187.

Moum, J., A. Perlin, J. Nash, and M. McPhaden, 2013: Seasonal sea surface cooling in the equatorial pacific cold tongue controlled by ocean mixing. *Nature*, **500**, 64–67, https://doi.org/10.1038/nature12363.

Price, J., R. Weller, and R. Pinkel, 1986: Diurnal cycling: Observations and models of the upper ocean's response to diurnal heating, cooling and wind mixing. *J. Geophys. Res.*, **91**, 8411–8427, https://doi.org/10.1029/JC091iC07p08411.

Reichl, B., and R. Hallberg, 2018: A simplified energetics based planetary boundary layer (ePBL) approach for ocean climate simulations. *Ocean Modell.*, **132**, 112–129, https://doi.org/10.1016/j.ocemod.2018.10.004.

——, and Q. Li, 2019: A parameterization with a constrained potential energy conversion rate of vertical mixing due to Langmuir turbulence. *J. Phys. Oceanogr.*, **49**, 2935–2959, https://doi.org/10.1175/JPO-D-18-0258.1.

Schultz, E., S. Josey, and R. Verein, 2012: First air-sea flux mooring measurements in the Southern Ocean. *Geophys. Res. Lett.*, **39**, L16606, https://doi.org/10.1029/2012GL052290.

Sullivan, P., J. McWilliams, and C. Moeng, 1994: A subgrid-scale model for large-eddy simulation of planetary boundary-layer flows. *Bound.-Layer Meteor.*, **71**, 247–276, https://doi.org/10.1007/BF00713741.

——, L. Romero, J. McWilliams, and W. Melville, 2012: Transient evolution of Langmuir turbulence in ocean boundary layers driven by hurricane winds and waves. *J. Phys. Oceanogr.*, **42**, 1959–1980, https://doi.org/10.1175/JPO-D-12-025.1.

Tennekes, H., 1973: A model for the dynamics of the inversion above a convective boundary layer. *J. Atmos. Sci.*, **30**, 558–567, https://doi.org/10.1175/1520-0469(1973)030<0558:AMFTDO>2.0.CO;2.

van Roekel, L., B. Fox-Kemper, P. Sullivan, P. Hamlington, and S. Haney, 2012: The form and orientation of Langmuir cells for misaligned winds and waves. *J. Geophys. Res.*, **117**, C05001, https://doi.org/10.1029/2011JC007516.

——, and Coauthors, 2018: The KPP boundary layer scheme: Revisiting its formulation and benchmarking one-dimensional ocean simulations relative to LES. *J. Adv. Model. Earth Syst.*, **117**, C05001, https://doi.org/10.1029/2018MS001336.

Wang, D., J. McWilliams, and W. Large, 1998: Large eddy simulation of the diurnal cycle of deep equatorial turbulence. *J. Phys. Oceanogr.*, **28**, 129–148, https://doi.org/10.1175/1520-0485(1998)028<0129:LESOTD>2.0.CO;2.

Watkins, C., and D. Whitt, 2020: Large-aspect-ratio structures in simlulated ocean surface boundary layer turbulence under a hurricane. *J. Phys. Oceanogr.*, **50**, 3561–3584, https://doi.org/10.1175/JPO-D-20-0134.1.

Wyngaard, J. C., 2010: *Turbulence in the Atmosphere*. Cambridge University Press, 393 pp.